Physica D : special issue

Buoyancy-Drag modelling of bubble and spike distances for single-shock Richtmyer-Meshkov mixing

David L Youngs [a,*], Ben Thornber [b]
[a] Department of Mechanical and Aerospace Engineering, University of Strathclyde, Glasgow G1 1XW, United Kingdom.
[b] School of Aerospace, Mechanical and Mechatronic Engineering, The University of Sydney, Sydney, Australia.

ABSTRACT

The Buoyancy-Drag model is a simple model, based on ordinary differential equations, for estimating the growth of a turbulent mixing zone at a interface between fluids of different density due to Richtmyer-Meshkov and Rayleigh-Taylor instabilities. The early stages of the mixing process are very dependent on the initial conditions and modifications to the Buoyancy-Drag model are needed to obtain correct results. In a recent paper, Youngs & Thornber [submitted to J. Fluids Eng. (2019)], the results of three-dimensional turbulent mixing simulations were used to construct the modifications required to represent the evolution of the overall width of the mixing zone due to single-shock Richtmyer-Meshkov mixing evolving from narrowband initial random perturbations. The present paper extends this analysis to give separate equations for the bubble and spike distances (the depths to which the mixing zone penetrates the dense and light fluids). The data analysis depends on novel integral definitions of the bubble and spike distances which vary smoothly with time. Results are presented for two pre-shock density ratios, $\rho_1 / \rho_2 = 3$ and 20. New insights are given for the variation of asymmetry of the mixing zone with time. At early time, values of the spike-to-bubble distance are very high. The asymmetry greatly reduces as mixing proceeds towards a self-similar state. For the overall (integral) mixing width, *W*, the Buoyancy-Drag model gives satisfactory results at both density ratios using the same parameters. However, for the bubble and spike distances the behaviour is very different at the two density ratios. The method used to analyse the data provides a new way of estimating the self-similar growth exponent θ ($W \sim t^{\theta}$). The values obtained are approximate because of the difficulty in running the three dimensional simulations far enough into the self-similar regime. Estimates of θ are consistent with the theoretical value of 1/3 given by the model of Elbaz & Shvarts [Physics of Plasmas (2018), 25, 062126]. The corrected form of the Buoyancy-Drag model gives accurate fits to the data for W, h_b and h_s over the whole time range with θ=1/3 for $\rho_1 / \rho_2 = 3$ and θ=0.35 for $\rho_1 / \rho_2 = 20$.

* Corresponding author.
E-mail address : david.youngs@strath.ac.uk

1. Introduction

Richtmyer-Meshkov (RM) instability occurs when a shock wave passes through a perturbed interface between fluids of different density. The related process, Rayleigh-Taylor (RT) instability, occurs when a light fluid accelerates a fluid of higher density. These two interface instabilities play an important role in many areas of research. They can degrade the performance of Inertial Confinement Fusion (ICF) capsules, see for example, Amendt et al. [1], Clark et al. [2]. They also occur in many astrophysical flows, Fryxell et al. [3]. Small initial interface perturbations form “bubbles” of light fluid which penetrate the dense fluid and “spikes” of dense fluid which penetrate the light fluid. The focus of the present paper is on modelling the formation, late-stage growth and spike-to bubble ratio of the RM turbulent mixing zone at high Reynolds number. A range of experiments and computer simulation techniques, Direct Numerical Simulation (DNS) and Large Eddy Simulation/ implicit Large Eddy simulation (LES/iLES) has been used to understand the turbulent mixing processes. For practical purposes engineering models, Reynolds-Averaged Navier-Stokes (RANS) models, are used to represent the turbulent mixing processes in complex flows. All of these experimental and numerical techniques are reviewed in detail by Zhou [4]. A very simple modelling approach is provided by the Buoyancy-Drag model. This uses ordinary differential equations to calculate the bubble and spike distances as functions of time. It continues to be a very useful model for giving a simple estimate of the amounts of mixing [1]. It also provides much insight into the mixing process and can help to fit the results of the complex mixing process into a simple pattern. Previous work on the Buoyancy-Drag model is also given in the review papers of Zhou.

The present paper uses results from iLES for validation of the Buoyancy-Drag model for single-shock RM mixing at pre-shock density ratios $\rho_1 / \rho_2 = 3$ and 20 . The cases considered here are limited to the use of narrowband initial random perturbations, as previously used in the “θ-group collaboration”, [5]. The earlier paper, Youngs and Thornber [6] used iLES results at $\rho_1 / \rho_2 = 3$ to show how the influence of initial conditions could be incorporated into the Buoyancy-Drag model for the integral mixing zone width, $W = \int \bar{f}_1 \bar{f}_2 dx$, where $\bar{f}_1$ and $\bar{f}_2$ denote the plane averaged fluid volume fractions. Data on the integral width was used as this quantity is insensitive to statistical

fluctuations. The method used to analyze the iLES data required the computation of dW/dt and d^2W/dt^2. The main purpose of the present paper is to extend the analysis to separate equations for the bubble and spike distances, h_b, h_s. To make this possible a novel method of defining integral bubble and spike distances has been devised which enables the required first and second derivatives to be calculated. The paper will discuss both the initialization of the model allowing for the effects of compressibility and non-linear saturation, and the subsequent growth of the mixing zone. For post-shock RM mixing at late time the mixing width varies as $W \sim t^{\theta}$ and for the narrowband case, when W becomes large compared to the initial perturbation scale, a self-similar state should be reached for which θ does not depend on the initial conditions. The variation of h_b, h_s with time is a matter of some controversy. According to the experimental results of Dimonte and Schneider [7], $h_b \sim t^{\theta_b}, h_s \sim t^{\theta_s}$ with $\theta_s > \theta_b$ at high density ratio. This implies that at late time $h_s / h_b \sim t^{\theta_s - \theta_b}$ where $\theta_s - \theta_b > 0$. Other papers, for example [5,8], have argued in favor of $\theta_s = \theta_b$ which gives $h_s / h_b = const.$ at late times which is analogous to the self-similar behaviour of RT mixing layers where the mixed width is proportional to t^2. The results derived here are used to calculate the variation of h_s / h_b with time at $\rho_1 / \rho_2 = 3$ and 20 and investigate this issue.

The layout of the paper is as follows. Section 2 summarizes previous work on the Buoyancy-Drag model and describes the equations used. The expected form of the modifications needed to represent the influence of the initial conditions is given in section 3. The new method for defining the integral bubble and spike distances is given in section 4. The iLES calculations used, at $\rho_1 / \rho_2 = 3$ and 20, are described in section 5 and the spike-to-bubble asymmetry is discussed in section 6. The analysis of the iLES data and the application of the Buoyancy-Drag model is given in section 7 for $\rho_1 / \rho_2 = 3$ and in section 8 for $\rho_1 / \rho_2 = 20$. At each density ratio, values of θ are found which give a consistent model for W, h_b and h_s. It is noted in the concluding remarks, section 9, that there is much scope for extending research, in particular the use of different forms for the initial conditions.

2. Previous research

The Buoyancy-Drag (BD) model is a simple heuristic model for mixing due to RM and RT instabilities at an interface between two fluids with densities $\rho_1 > \rho_2$. An acceleration, *g*, normal to the interface (which need not be constant) drives the instability. For finite *g* > 0, RT instability occurs. An impulsive acceleration corresponds to RM instability. If mix velocities are small compared to the sound speeds (which is true for the cases considered here), the flow becomes near- incompressible soon after shock transit, on a time-scale which is very short compared to the mixing time scale. The instability at a plane boundary between incompressible fluids is considered here. Ordinary differential equations are used to calculate the time variation of h_b and h_s, the distances to which the instabilities penetrate the dense and less dense fluids (the bubble distance and the spike distances).

The model is based on the initial work of Layzer [9] and Baker and Freeman [10]. Layzer's equation for the bubble evolution from a single sinusoidal mode with wavelength λ at $\rho_2 = 0$ may be written in the form:-

$$\left(2+E\right)\frac{dV_b}{dt} = \left(1-E\right)g - 6\pi\frac{V_b^2}{\lambda}$$
$$\frac{dh_b}{dt} = V_b \qquad E = \exp\left(-\frac{6\pi h_b}{\lambda}\right) \qquad \text{..... (1)}$$

This gives the correct small-amplitude behavior

$$\frac{d^2h_b}{dt^2} = \frac{2\pi g}{\lambda}h_b \qquad \text{.....(2)}$$

At $\rho_2 = 0$ the spike freely accelerates giving $h_s \sim \frac{1}{2}gt^2$ (if g is constant)

Layzer's equation for the bubble distance can be interpreted as having the form: mass × acceleration = buoyancy force – drag. Baker and Freeman recognized that for $\rho_2 \neq 0$ "drag" on the spikes needed to be included and constructed buoyancy-drag equations for both spikes and bubbles for single mode RT instability. For turbulent mixing, there may be an initial dominant scale determined by the initial conditions but at late time the length scale should increase in proportion to the width of the mixing zone. The model was extended to represent turbulent mixing by Hansom et al. [11]. The equations used for the bubble and spike velocities were

$$\frac{dV_b}{dt} = Ag - C_D \frac{V_b^2}{\ell}$$
$$\frac{dV_s}{dt} = Ag - C_D \left(\frac{\rho_2}{\rho_1}\right)^p \frac{V_s^2}{\ell} \qquad \text{.....(3)}$$

where $\ell = h_b$ at late time. For constant *g* there is a self-similar solution with $h_b = \alpha A g t^2$ where $\alpha = 1/(2 + 4C_D)$ which has been indicated by many experimental investigations, for example [7,12]. The exponent *p* , which models the reduced drag on the spikes, is chosen to match experimental estimates of h_s / h_b .

A slightly different form of the Buoyancy-Drag model has been used by Dimonte and Schneider [7]:

$$\frac{dV_b}{dt} = \beta_b Ag - C_b \frac{V_b^2}{h_b}$$
$$\frac{dV_s}{dt} = \beta_s Ag - C_s \frac{V_s^2}{h_s} \qquad \text{.....(4)}$$

The β- factors, typically < 1, may be thought of as modelling a reduction in the buoyancy force due to fine-scale mixing and give extra degrees of freedom for matching experiments with time-varying accelerations.

Equations (3) and (4) give similar behavior for RT mixing. The Buoyancy-Drag model represents RM mixing as an impulsive acceleration which generates the initial bubble and spike velocities followed by decay due to drag with *g* = 0 and in this case (3) and (4) give qualitatively different behavior. Equation (3) which uses the same length scale in the bubble and spike equations, gives self-similar behavior at late-time with h_b and $h_s \sim t^\theta$ where $\theta = 1/(1 + C_D)$ (unless $\rho_2 = 0$) and $h_s / h_b \sim (\rho_1 / \rho_2)^p$. On the other hand, equation (4), allows for different values of θ for bubbles and spikes, $\theta_b = 1/(1 + C_b)$, $\theta_s = 1/(1 + C_s)$. In some of the variable acceleration experiments of [7] a very high acceleration was applied for a short time to create a layer of turbulent mixing. Mixing then evolved with *g* = 0 thus representing the decay stage of the RM process. At $\rho_1 / \rho_2 = 3$ it was found that $\theta_s \sim \theta_b$ but at higher density ratios h_s / h_b increased with time and this suggested $\theta_s > \theta_b$. The values of $\theta_b = 0.25 \pm 0.05$ showed little variation with density ratio. In these experiments the initial layer of RT turbulence has a dominant length scale and it could be argued that this corresponds to a highly non-linear

narrowband initial perturbation. A summary of previous estimates of θ up to 2017, for both narrowband and broadband initial conditions, is given in the review paper of Zhou, [4], part 1, table 6.4. Several other experiments [13-15] have given higher values of θ which may be due to broadband initial conditions. In most cases separate values for θ_b and θ_s are not measured but in the shock tube experiments of Krivets et al. [15] at Atwood number 0.7, separate values were measured. A wide range of values of θ, 0.2 to 0.6, was reported (attributed to variations in the initial conditions). However, similar values were found for θ_b and θ_s . Recent high-resolution narrowband simulations [5] (the "quarter-scale case") have indicated θ ~ 0.29, based on the results of 7 different iLES algorithms. For the narrowband case, theoretical models have given θ =0.25 at very low Atwood number [16] (EDQNM model) and θ=1/3 [17] (bubble merger model).

The buoyancy-drag model has also been used by Alon et al. [18] and Kartoon et al. [19]. The equation for the bubble velocity is

$$\left(\rho_2 + c_a\rho_1\right)\frac{dV_b}{dt} = \left(\rho_1 - \rho_2\right)g - c_D\rho_1\frac{V_b^2}{\lambda} \qquad \text{.....(5)}$$

c_a and c_D are added mass and drag coefficients and λ is the mean wavelength of the bubbles. It was argued in [18] that when the bubble evolution becomes self-similar the spikes have not yet reached their asymptotic velocity. This led to a model with $\theta_s > \theta_b$ which gave a good match to the experimental data [7].

The volume fraction profiles obtained from the iLES results [5,8] indicated self-similar behavior with h_s / h_b tending towards a constant value at late time due to collapse of the plane averaged volume fractions with a single length scale. It was assumed that $\theta_s = \theta_b$ and that the common value of θ was appropriate for the late time behavior of the integral width *W*. The variation of h_s / h_b with time will be investigated in more detail in this paper in an attempt to resolve the differing views on this matter. The Buoyancy-Drag modelling in sections 7 and 8 will assume $\theta_s = \theta_b$.

An alternative model, similar to the Buoyancy-Drag model was derived by Ramshaw [20]. An equation of motion for *h*, the half-width of the mixing zone was derived using Lagrange's equations. This modelled both the early time behavior, assuming a dominant wavelength set by the initial conditions, and an asymptotic late-time behavior. For incompressible mixing with constant densities, at late time:-

$$h\dot{V} + \frac{1}{2}V^2 + \frac{2\pi c}{b}|V|V - \frac{2\pi Ag}{b}h = 0 \qquad \text{.. (6)}$$

where $V = \dot{h}$ and b and c are model coefficients.

This has the same form as the Buoyancy-Drag model (if de-mixing, $V < 0$, does not occur) but there is a key difference of interpretation. In the absence of dissipation ($c = 0$) and gravity ($g = 0$), the equation reduces to

$$h\dot{V} + \tfrac{1}{2}V^2 = 0 \quad \text{i.e. energy is conserved } \frac{d}{dt}\left(hV^2\right) = 0 \qquad \ldots(7)$$

Hence part of the V^2 - terms in the Buoyancy-Drag model should be attributed to conservation of kinetic energy.

3. Modifications to the Buoyancy-Drag model

Mixing in complex flows often begins with a shock wave passing through the interface. This amplifies the initial perturbations. Mixing is then enhanced by subsequent shock waves and periods of RT instability. The first shock may only cause a small fraction of the final amount of mixing but it does set the initial conditions for the subsequent mixing processes. Modifications to the buoyancy-drag model are needed to take account of the initial perturbations present when the first shock reaches the interface. Reference [6] described modelling of the growth of integral mixing zone width from narrow-band initial perturbations for a pre-shock density ratio of $\rho_1 / \rho_2 = 3$. The standard deviation of the initial perturbation was given by $\sigma_0^2 = \int P(k)dk$ where $P(k) =$ a constant for $2\pi/\lambda_{\max} = k_{\min} < k < k_{\max} = 2\pi/\lambda_{\min}$. In the present paper the analysis is extended to modelling the bubble and spike distances as well as the integral width and also considers a higher density ratio of $\rho_1 / \rho_2 = 20$ using an identical form of initial perturbations.

At late time, when self-similar mixing is assumed, the Buoyancy-Drag model (3) is written in the form

$$\frac{dW}{dt}=V,\quad \frac{dV}{dt}=-c_D\frac{V^2}{W}$$
$$\frac{dh_b}{dt}=V_b,\quad \frac{dV_b}{dt}=-c_D\frac{V_b^2}{h_b} \qquad \ldots(8)$$
$$\frac{dh_s}{dt}=V_s,\quad \frac{dV_s}{dt}=-c_D\frac{V_s^2}{Rh_b}$$

Where R is the asymptotic value of h_s/h_b.

However, as the mixing zone width is initially small, the drag terms are far too high immediately after shock passage and modified forms are needed:-

$$\frac{dV}{dt}=-c_D\frac{V^2}{\ell},\quad \frac{dV_b}{dt}=-c_D\frac{V_b^2}{\ell_b},\quad \frac{dV_s}{dt}=-c_D\frac{V_s^2}{\ell_s} \qquad \ldots(9)$$
$$\text{with } \ell=\ell\left(\bar{\lambda},W\right),\ \ell_b=\ell_b\left(\bar{\lambda},h_b\right),\ \ell_s=\ell_s\left(\bar{\lambda},h_b\right)$$

At late time $\ell=W$, $\ell_b=h_b$, $\ell_s=Rh_b$. $\bar{\lambda}$ is a suitably defined mean initial perturbation wavelength. The required variation of the length scales with time is found from the iLES data for W, h_b and h_s versus time by numerical differentiation:-

$$\ell^{eff}=\frac{\ell}{C_D}=-\frac{V^2}{dV/dt},\ \ell_b^{eff}=\frac{\ell_b}{C_D}=-\frac{V_b^2}{dV_b/dt},\ \ell_s^{eff}=\frac{\ell_s}{C_D}=-\frac{V_s^2}{dV_s/dt} \qquad \ldots\ldots(10)$$

It should be noted that in the RM experiments of Dimonte and Schneider [7] the flow is initialized with a layer of RT created turbulence. It this case $\ell=W$ is a reasonable approximation the start of the RM process and the modifications to the buoyancy-drag model described here are not applicable.

As in [6], the expected behavior of the mixing zone may be divided into four stages, as given below.

(1) Impulsive acceleration

The first step is to estimate the initial post shock mix velocities. According to [5,6], if the initial response is in the linear regime, the initial value of $\dot{W}$ should be given by

$$V_0^{theory}=\dot{W}_0=0.564\sigma_0^+\bar{k}\left|A^+\Delta u\right| \quad \text{where } \sigma_0^+=C\sigma_0 \qquad \ldots\ldots(11)$$

and $\bar{k}=2\pi/\bar{\lambda}$ where $\bar{\lambda}=\sqrt{\frac{12}{7}}\lambda_{\min}$ is the appropriate mean wavenumber for the narrowband multimode perturbation. σ_0^+ is the compressed (post-shock) value of the

standard deviation of the perturbation, σ_0, and A^+ denotes the post-shock Atwood number . The correction for compressibility, which does not depend on wavelength, can be estimated, for example, from the approximate theories of Richtmyer [21] , Meyer and Blewitt [22] or Vandenboomgaerde et al. [23] or by performing a 2D single mode simulation. For the initial bubble and spike velocities a different numerical factor is needed in equation (11). This will be discussed in the next section. It is apparent from the analysis of the iLES data, sections 7 and 8, that corrections for non-linearity are also needed in equation (11) for the initial conditions used here.

The subsequent behavior can be divided into three further stages:-

(2) Weakly non-linear stage

The Layzer equation (1), assuming E=0 suggests, for A=1

$$\frac{dV_b}{dt} = -3\pi \frac{V_b^2}{\bar{\lambda}} \qquad \ldots(12)$$

Initially the width of the turbulent kinetic energy region is $W_k \sim \bar{\lambda}$. Hence energy conservation, equation (7) gives

$$\frac{d}{dt}\left(\tfrac{1}{2} W_K V^2\right) = 0 \Rightarrow \frac{dV}{dt} \sim -\tfrac{1}{2}\frac{V^2}{W_K} \qquad \ldots(13)$$

Both of these results indicate $\ell, \ell_b, \ell_s \sim \bar{\lambda}$ immediately after the peak initial mix velocities are achieved.

(3) Initial turbulent stage

For the multimode case (assuming high Reynolds number), an inertial range is expected to form after time $\sim \frac{\bar{\lambda}}{V_0}$. A dissipation term then needs to be included in equation (13) as in the Ramshaw model, equation (6):-

$$\frac{d}{dt}\left(\tfrac{1}{2} W_K V^2\right) = -C_{diss}\frac{V^3}{\bar{\lambda}} W_K \Rightarrow \frac{dV}{dt} \sim -\tfrac{1}{2}\frac{V^2}{W_K} - C_{diss}\frac{V^2}{\bar{\lambda}} \qquad \ldots(14)$$

Again $\ell, \ell_b, \ell_s \sim \bar{\lambda}$ is expected but with lower values than in the weakly non-linear stage. Here it is expected that the effective length scale

$$\ell \sim -\frac{V^2}{dV/dt} \sim \frac{\bar{\lambda}}{\bar{\lambda}/(2W_k) + C_{diss}}. \qquad \ldots\ldots(15)$$

(4) Asymptotic turbulent stage.

At late time the length scale will increase in proportion to the mixing zone width giving $\ell = W$, $\ell_b = h_b, \ell_s = R\ell_s$, as noted above.

The length scales should initially have finite values, $\propto \bar{\lambda}$, drop to lower values, also related to $\bar{\lambda}$, and finally increase in proportion to W or h_b.

For 2D single mode simulations, for example Probyn et al. [24], it is known that, at high Atwood number, the bubble velocity decays more rapidly than the spike velocity. A vortex pair forms on the spike side and this decelerates at a relatively slower rate. For the multimode case, as there is a dominant initial scale, similar behavior is expected. This suggests $\ell_s > \ell_b$ in the early stages.

4. Definition of bubble and spike distances

For the analysis used in this paper, a definition of the bubble and spike distances, h_b and h_s, is needed which can be differentiated twice with respect to time. For the overall amount of mixing it is possible to use either the integral width, $W = \int \bar{f}_1 \bar{f}_2 dx$, as in [6] or the integral mix mass $M = \int \bar{\rho} \tilde{m}_1 \tilde{m}_2 dx$ as proposed by Zhou et al. [25]. The latter reference discussed the merits of using the integral mass for mixing in compressible flows. However, there are merits in using volume fractions for incompressible mixing (as being considered here). For Rayleigh-Taylor mixing with $Ag =$ a constant , Youngs [26,27], showed that volume fractions distributions do not show a large variation with density ratio whereas mass fraction distributions would. For two-fluid mixing, the bubble and spike positions can reasonably be defined as the points where $\bar{f}_1 = 0.99$ and 0.01. At high density ratio the mass fraction, $\tilde{m}_1$, is close to unity throughout the mixing zone and suitable cut-off values would need to depend on the density ratio.

If post-shock RM mixing is incompressible the density of the mixture is $\rho = f_1\rho_1^+ + f_2\rho_2^+$, where ρ_1^+ and ρ_2^+ are the post-shock densities. However, the compressible iLES calculates mass fractions and compressibility has a small effect after shock passage. Using the mass fractions, m_r , for species *r*, the volume fractions are then defined as $f_r = \left(m_r / \rho_r^+\right) / \left(m_1 / \rho_1^+ + m_2 / \rho_2^+\right)$.

The integral bubble and spike distances used here are defined as follows. A bi-linear volume fraction distribution, with bubble volume = spike volume, is considered:-

$$\bar{f}_1 = \begin{cases} 1-(1-f_l)\left(1+\dfrac{x}{h_b}\right) & \text{for } -h_b < x < 0 \\ f_l\left(1-\dfrac{x}{h_s}\right) & \text{for } 0 < x < h_s \end{cases} \qquad \text{where } f_l = \frac{h_b}{h_b + h_s} \qquad ..(16)$$

The integral bubble and spike distances are defined as weighted average distances from the interface of the bubble fluid for $x < 0$ and the spike fluid for $x > 0$. For example, the spike height may be written as:-

$$\int_0^\infty x^m f dx = \frac{f_l h_s^{m+1}}{(m+1)(m+2)} \qquad .....(17)$$

An explicit evaluation of the interface value of the bilinear distribution, f_l ,is not required if the heights are written as follows:-

$$\bar{h}_b^{(m)} = \left[\frac{(m+1)(m+2)}{2} \frac{\int_{-\infty}^{0} |x|^m \left(1-\bar{f}_1\right) dx}{\int_{-\infty}^{0} \left(1-\bar{f}_1\right) dx} \right]^{\frac{1}{m}} \qquad \bar{h}_s^{(m)} = \left[\frac{(m+1)(m+2)}{2} \frac{\int_0^{\infty} x^m \bar{f}_1 dx}{\int_0^{\infty} \bar{f}_1 dx} \right]^{\frac{1}{m}} \qquad ...(18)$$

The values are scaled so that $\bar{h}_b^{(m)} = h_b$, $\bar{h}_s^{(m)} = h_s$ for the bi-linear distribution. Integral bubble and spike distances for $m = 1,2,3$ are considered here.

In order to analyze the early time data when the instability is in the linear regime, integral mix widths, bubble and spike distances are needed to two specific cases. For a single – mode distribution with amplitude *a*, the volume fraction distribution and integral distances (obtained by numerical integration of equation (18)) are given by

$$\bar{f}_1(x) = \frac{1}{2}\left(1 - \frac{2}{\pi}\sin^{-1}\frac{x}{a}\right)$$
$$W = 0.4053a$$
$$\bar{h}_b^{(1)} = \bar{h}_s^{(1)} = 1.1781a \qquad ....(19)$$
$$\bar{h}_b^{(2)} = \bar{h}_s^{(2)} = 1.1547a$$
$$\bar{h}_b^{(3)} = \bar{h}_s^{(3)} = 1.1378a$$

For the Gaussian multimode random initial perturbations, the volume fraction distribution is given by the error function. If σ is the standard deviation of the height distribution the results obtained are

$$\bar{f}_1(x) = \frac{1}{2}\left(1 - erf\frac{x}{\sqrt{2}\sigma}\right)$$
$$W = 0.5642\sigma$$
$$\bar{h}_b^{(1)} = \bar{h}_s^{(1)} = 1.880\sigma \qquad \text{.....(20)}$$
$$\bar{h}_b^{(2)} = \bar{h}_s^{(2)} = 2.0\sigma$$
$$\bar{h}_b^{(3)} = \bar{h}_s^{(3)} = 2.110\sigma$$

In order to calculate the bubble and spike distances it is essential to locate the centre of the mixing zone x_c (set to zero above). In the FLAMENCO simulations there is some motion of the mixing zone relative to the mesh and this leads to some ambiguity in locating the mixing zone centre. The method used here is to assume incompressible mixing and to locate the mixing zone centre by equating bubble and spike volumes:-

$$vol_b(x_c) = vol_s(x_c)$$

where $vol_b(x) = \int_{-\infty}^{x}\left(1 - \bar{f}_1(x')\right)dx'$

$$vol_s(x) = \int_{x}^{\infty}\bar{f}_1(x')dx'$$

It follows that $vol_b(x) - vol_s(x) = x - x_c$. Hence linear interpolation to get $vol_b(x_c) = vol_s(x_c)$ should give an accurate estimate for the location of mixing zone center.

5. Implicit large eddy simulations

The results of three-dimensional iLES are used to provide the data for the analysis of the Buoyancy-Drag model. The algorithm used is FLAMENCO, a fifth-order in space, second order in time algorithm developed at the University of Sydney [28,29]. Youngs and Thornber [6] gave an analysis of the integral with data from FLAMENCO and other numerical techniques which were used in the θ-group collaboration [5]. The pre-shock density ratio was $\rho_1 / \rho_2 = 3$. The present paper extends the analysis to modelling of the bubble and spike distances and also considers a higher pre-shock density ratio, $\rho_1 / \rho_2 = 20$. In both cases the adiabatic index for both fluids is γ = 5/3 and the shock wave travels from the dense fluid to the light fluid. The shock conditions taken from [8] are listed in table 1.

Table 1: shock conditions

	Low Atwood number	High Atwood number
ρ_1	3.0	20.0
ρ_2	1.0	1.0
ρ_1^+, post shock density	5.22	25.75
ρ_2^+, post shock density	1.80	1.415
incident shock Mach number in dense fluid	1.8439	1.91
U_s, incident shock speed	291.575	174.36
Δu, change in interface velocity	434.6	155.55

Two new calculations are used for the late time behaviour:-

(a) Low Atwood number $\rho_1 / \rho_2 = 3$:The initial conditions are similar to the quarter scale case in [5] but the calculation is run to a much later stage to get a better estimate of the asymptotic behaviour. This is made possible by reducing the resolution of the initial perturbation wavelengths ($\lambda_{\min} = 12\Delta x$ is used instead of $\lambda_{\min} = 16\Delta x$) and increasing the perturbation amplitude from $\sigma_0 = 0.1\lambda_{\min}$ to $\sigma_0 = 0.2\lambda_{\min}$ (this leads to higher initial velocities and asymptotic behaviour at an earlier time). The pre-shock pressures are 1x10^5 Pa, and the computation is run through to a dimensional time of 5 s.

To accommodate later time growth the domain length was increased moderately from 2.8π to 3π, thus the x-direction mesh count was increased in proportion to maintain an equal mesh quality to the θ-group case. The mesh size was 896 x 512 x 512. It was noted in [6] that reflections from the mesh boundaries led to unwanted oscillations in the second derivatives d^2W/dt^2 . These were significantly reduced in these computations by overwriting the transmitted shock and associated boundary region with the analytical post-transmitted shock values just prior to it exiting the refined region of the computational domain.

As in [5] a slightly diffuse initial interface was used where the diffusion thickness $\delta = \lambda_{\min}/4$. It was shown in [6] that this has little effect at late time. From simple scaling this modified test case enabled a simulation of an RM layer to approximately double the dimensionless time with available computational power and without the finite domain

size influencing the growth of the integral width (The effect of finite domain size was investigated in [30]).

(b) High Atwood number: The mesh resolution was chosen to give $\lambda_{\min} = 16\Delta x$ and for the perturbation amplitude $\sigma_0 = 0.1\lambda_{\min}$ was used. The perturbation spectrum and coefficients are exactly identical to the lower Atwood θ-group quarter scale test case. This minimum wavelength of $\lambda_{\min} = 16\Delta x$ was chosen as the higher Atwood case is more challenging to resolve than the At=0.5 case. The domain length has been moderately extended to 3π as it is expected that the spikes will be longer than the equivalent At=0.5 case, and the mesh size was 896 x 512 x 512. The pre-shock pressures are 1×10^5 Pa, and the computation is run through to a dimensional time of 4.2 s.

As for the low Atwood number calculation, a slightly diffuse initial interface was used. It was noted that both the reflected rarefaction and transmitted shock triggered very weak reflected waves while exiting the boundary which impacted the computation of *dV/dt*. Thus for the At=0.9 case both the reflected rarefaction and transmitted shocks were over-written by the analytical solution just prior to exiting the x-boundaries, which reduced reflections by two orders of magnitude. Given equal compression factors, the specified initial conditions detailed in table 1 would give the same initial growth rates for both Atwood numbers, however, due to a higher compression factor for the At=0.9 case the estimated initial growth rate is moderately lower by a factor of ~15%.

For both of the new calculations for the late time behavior there are regions of lower mesh resolution in the *x*-direction near the boundaries. The mix region width, $h_b + h_s$, as defined here which corresponds approximately to the 1% volume fraction limits, fills about 50% of the refined mesh region in the *x*-direction and should not be significantly affected by the finite domain size.

As in the earlier FLAMENCO simulations an initial velocity of $-\Delta u$ is given to the gas interface such that the centre of the interface is stationary after shock passage. The results from the above simulations should give accurate results at late time when the mixing zone is well resolved. Higher resolution FLAMENCO simulations have been performed to obtain accurate results for the very early time behaviour. These have used the same domain size but with double the grid resolution in each direction, being 1568 x 1024 x 1024. For the early time computations, the minimum wavelength has also been increased such that the perturbation is substantially better resolved. Note that the perturbation is statistically identical but the actual form is different, which means that an

exact correspondence is not expected. High resolution single-mode calculations are also used to derive the compression factor, *C*, in equation (11).

Table 2 summarizes the multimode simulations used in this paper, including those from [5]. The extent to which a calculation has reached the final self-similar state is measured by the dimensionless time $\tau = V_0^{theory} t / \bar{\lambda}$, where V_0^{theory} and $\bar{\lambda}$ are given by equation (11). The maximum values of τ reached are listed in table 2. In this case *t* is measured from the time when the perturbation inverts (as used in figure 8, for example).

Table 2: multimode simulations

Calculation number	ρ_1 / ρ_2	λ_{min}	σ_0	δ	mesh size	τ_{max}
#1,2,3*	3.0	$16\Delta x$	$0.1\lambda_{min}$	$\lambda_{min}/4$	720 x 512 x 512	430
#4	3.0	$12\Delta x$	$0.2\lambda_{min}$	$\lambda_{min}/4$	896 x 512 x 512	1150
#5	3.0	$96\Delta x$	$0.05\lambda_{min}$	0.0	1568 x 1024 x 1024	0.26
#6	3.0	$96\Delta x$	$0.1\lambda_{min}$	0.0	1568 x 1024 x 1024	0.51
#7	3.0	$96\Delta x$	$0.1\lambda_{min}$	$\lambda_{min}/4$	1568 x 1024 x 1024	0.51
#8	3.0	$96\Delta x$	$0.2\lambda_{min}$	0.0	1568 x 1024 x 1024	0.97
#9	3.0	$96\Delta x$	$0.2\lambda_{min}$	$\lambda_{min}/4$	1568 x 1024 x 1024	0.97
#10	20.0	$16\Delta x$	$0.1\lambda_{min}$	$\lambda_{min}/4$	896 x 512 x 512	344
#11	20.0	$128\Delta x$	$0.1\lambda_{min}$	0.0	1568 x 1024 x 1024	0.33
#12	20.0	$128\Delta x$	$0.1\lambda_{min}$	$\lambda_{min}/4$	1568 x 1024 x 1024	0.33
#13	20.0	$64\Delta x$	$0.1\lambda_{min}$	$\lambda_{min}/4$	1568 x 1024 x 1024	0.69

* #1,2,3 refer to the quarter scale, FLAMENCO, TRICLADE and TURMOIL calculations described in [5] for which only data for *W* versus time is available. The rest are the new calculations using FLAMENCO.

6. Bubble to Spike asymmetry

Figures 1 and 2 show three-dimensional iso-surfaces of volume fraction and two-dimensional contour floods of volume fraction on a single plane from the θ-group quarter scale case perturbation at ρ_1/ρ_2=3 and at ρ_1/ρ_2=20. These two cases are chosen as the initial perturbations are identical. Two times are shown, an early time (t=0.025 s for ρ_1/ρ_2=3 and t=0.03 s for ρ_1/ρ_2=20) and a later time (t=2 s for ρ_1/ρ_2=3 and t=2.4 s for ρ_1/ρ_2=20), where the differences in physical time approximately account for the difference in the initial impulse thus the plots are at similar non-dimensional times. From these visualisations it is clear that qualitatively there is a substantial influence of the Atwood number at early time, particularly on the spike side, however a diminishing influence at late time. There is less asymmetry between the spike and bubble side at low Atwood number. The spikes in the low Atwood case have a lower aspect ratio as on average they have not travelled as deeply into the lighter fluid. Furthermore, there is lower mixing at the bubble tips.

At late time the distinction between the two Atwood numbers is not as great. The spike to bubble amplitude is higher at At=0.9 (most visible in the slices in figure 2), however both layers are progressing towards a fully developed turbulent mixing layer. At both times the morphology of the bubble side is qualitatively relatively insensitive to Atwood number.

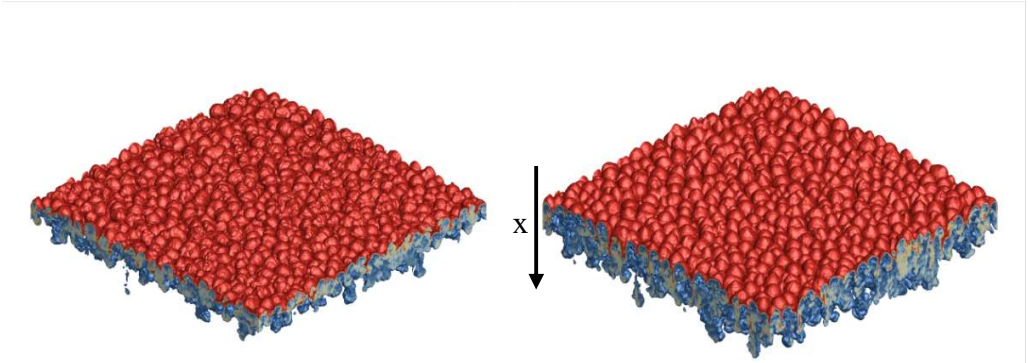

(a) At=0.5, t=0.025 s, W/$\bar{\lambda}$=0.43 At=0.9, t=0.03 s, W/$\bar{\lambda}$=0.37s

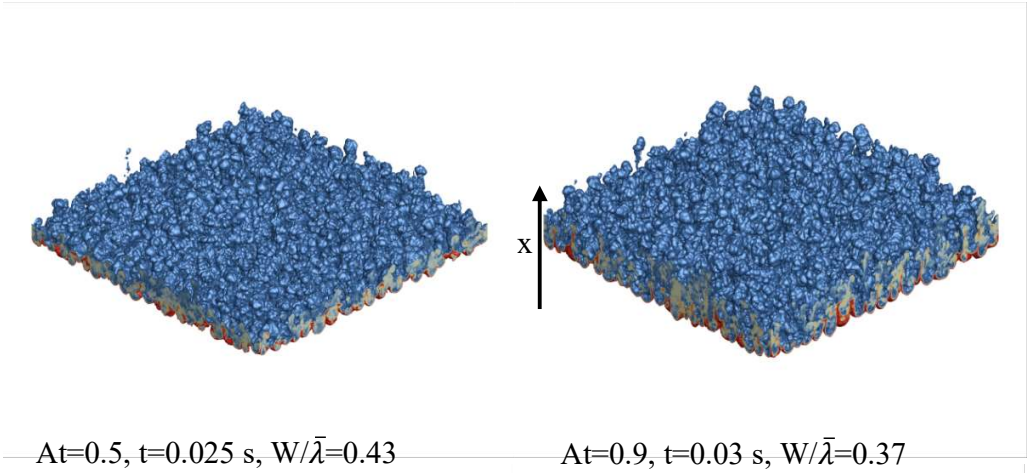

(b) At=0.5, t=0.025 s, W/$\bar{\lambda}$=0.43 At=0.9, t=0.03 s, W/$\bar{\lambda}$=0.37

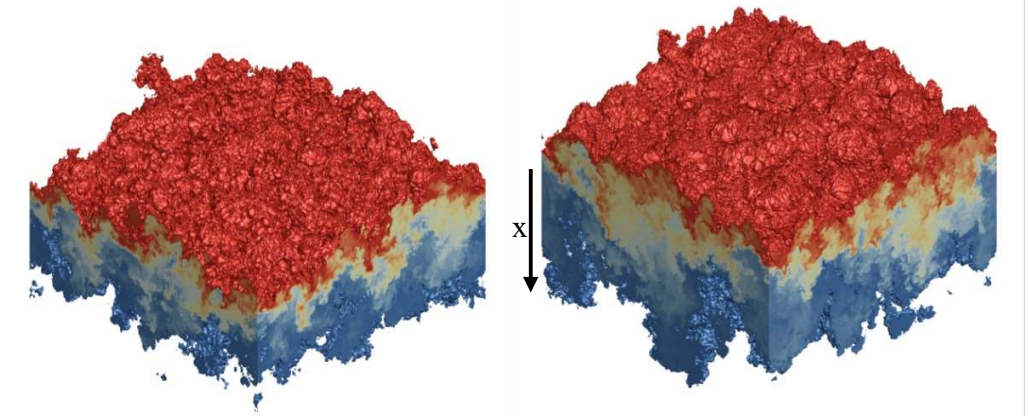

(c) At=0.5, t=2 s, W/$\bar{\lambda}$=1.34 At=0.9, t=2.4 s, W/$\bar{\lambda}$=1.40

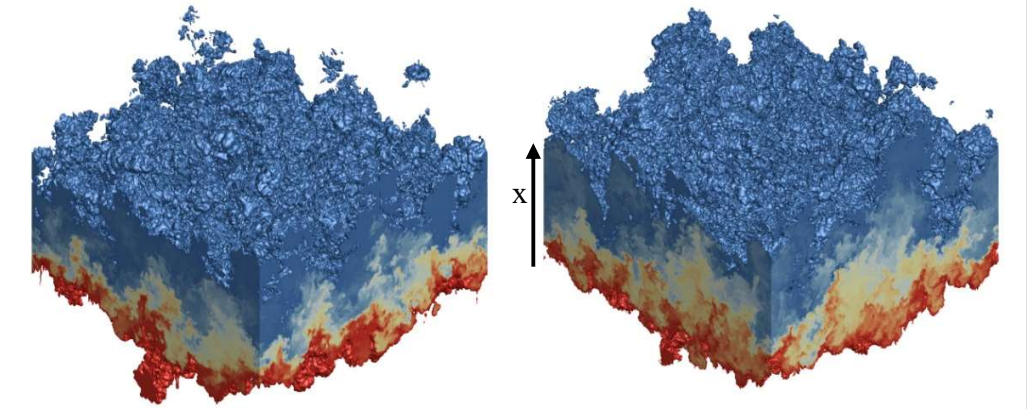

(d) At=0.5, t=2 s, W/$\bar{\lambda}$=1.34 At=0.9, t=2.4 s, W/$\bar{\lambda}$=1.40

Fig. 1: Visualisation of iso-surfaces of volume fraction for At=0.5, calculation #1 (left) and At=0.9, calculation #10 (right) at (a) bubble side, early time (t=0.025 s for At=0.5 and 0.03 s for At 0.9) (b) spike side, early time, (c) bubble side, late time (t=2 s for At=0.5 and 2.4s for At=0.9) and (d) spike side, late time. Note that the image is rotated such that positive x points downwards in the bubble visualisation and upwards on the spike side. Note that at early times the light fluid volume fraction isosurfaces 0.01 and 0.99 are shown, at late time it is changed to 0.999 and 0.001 to capture the spike structure.

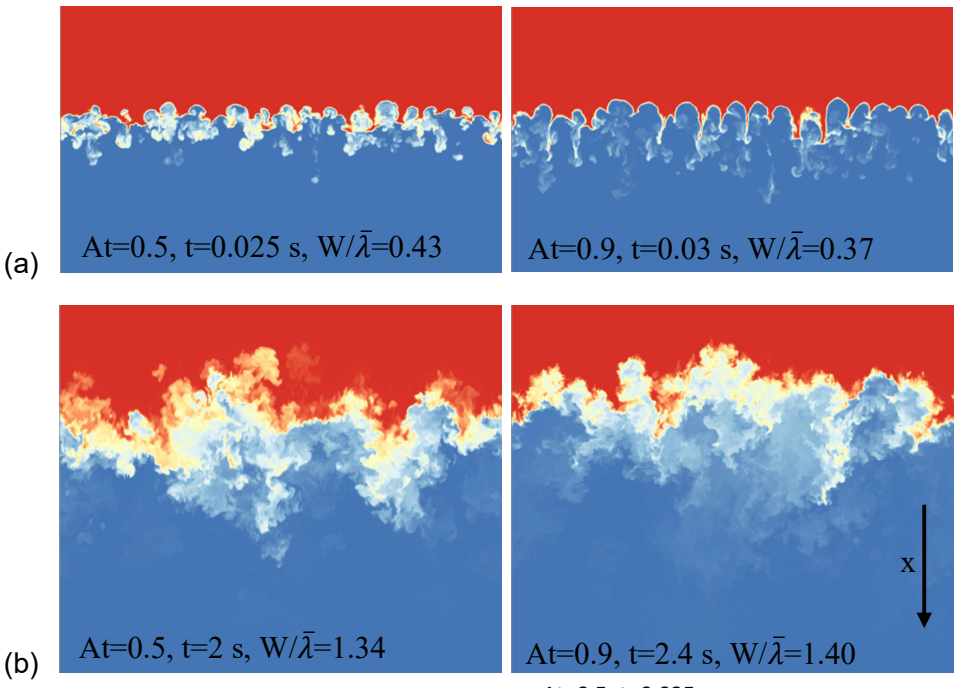

Fig. 2: Visualisation of a single slice showing contours of volume fraction for At=0.5,calculation #1 (left) and At=0.9, calculation #10 (right) at (a) early time (t=0.025 s for At=0.5 and 0.03 s for At 0.9), and (b) late time (t=2 s for At=0.5 and 2.4s for At=0.9). Note that this does not show the full computational domain, and the image is rotated such that positive x points downwards.

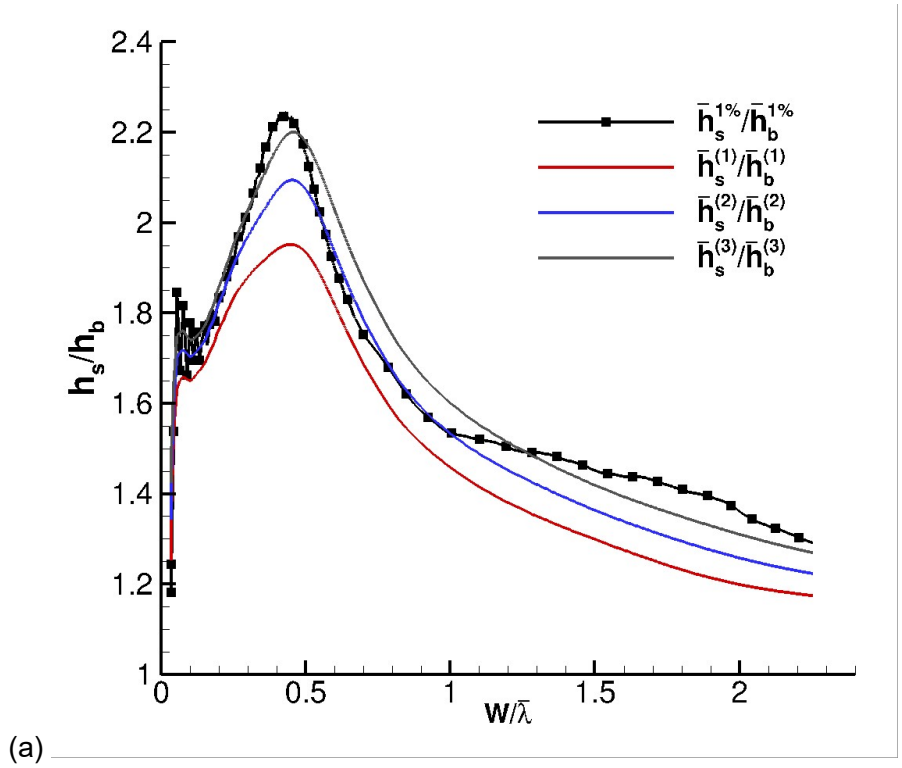

(a)

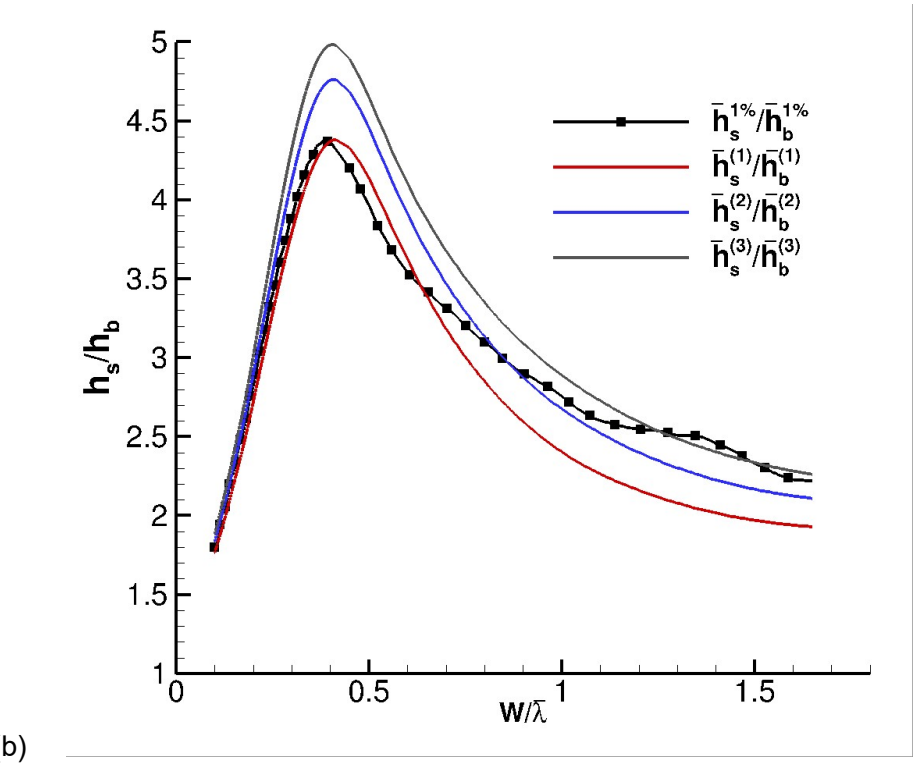

(b)

Fig. 3: Variation of spike to bubble ratio, h_s / h_b, versus $W / \bar{\lambda}$ at (a) $\rho_1 / \rho_2 = 3$, calculation #4 and (b) $\rho_1 / \rho_2 = 20$, calculation #10.

Figure 3 shows plots of the spike to bubble ratio, h_s / h_b, versus $W / \bar{\lambda}$ at the two density ratios. Values of $\bar{h}_s^{(m)} / \bar{h}_b^{(m)}$ derived from the integral measures are compared with spike to bubble ratios derived from the 1% and 99% volume fraction limits, $h_s^{1\%} / h_b^{1\%}$. The integral measures behave in a very similar way to the bubble and spike distances derived from volume fraction cut-offs (which are affected by fluctuations). At early time a very high degree of asymmetry is found. This is attributed to the formation of vortex rings on the spike side which initially propagate with near constant velocity and take a long time to break up. As already noted, 2D single mode calculations show a similar degree of asymmetry (vortex pair rather than vortex ring). It is difficult to explain early time asymmetry by increased drag on the spikes by a factor ~ ρ_1 / ρ_2. In the buoyancy-drag modelling it will prove necessary to assume that dissipation is much lower on the spike side than on the bubble side at early time.

Towards the end of the simulations h_s / h_b drops to much lower values. It is apparent from these results that $\theta_s > \theta_b$ is not appropriate for these cases and a common value of θ will be used in sections 7 and 8 for modelling h_b and h_s. Scaled volume fraction distributions are shown in figure 4.

(a)

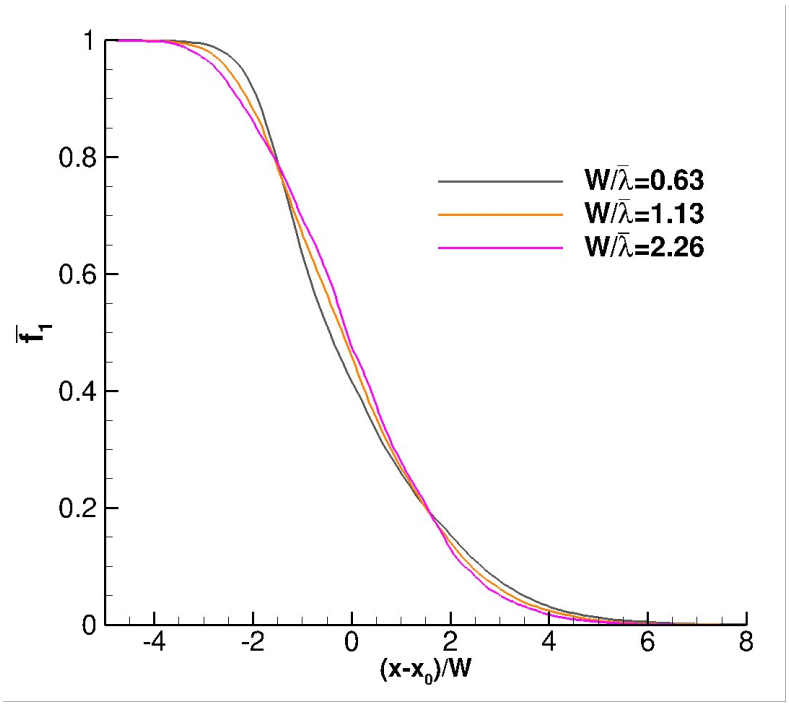

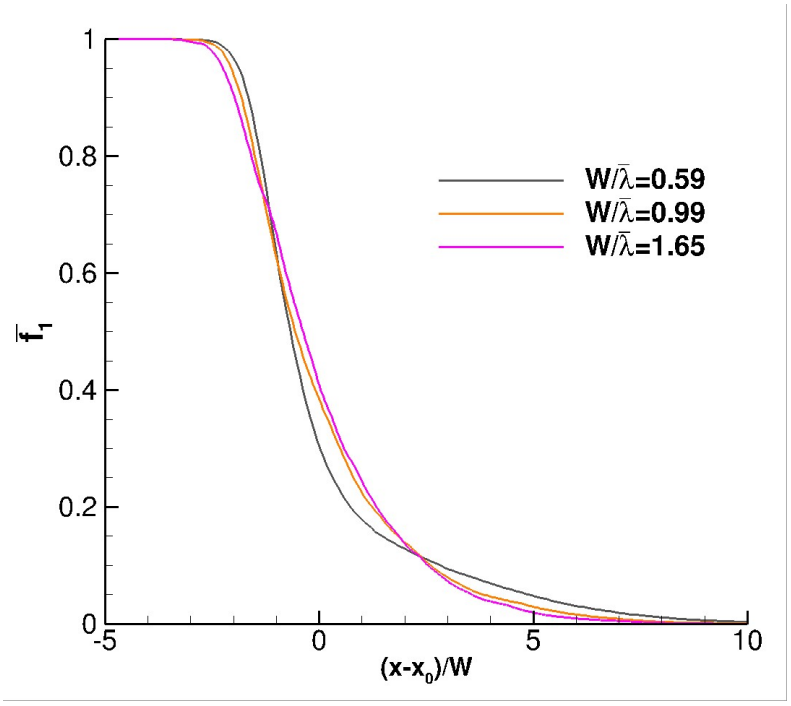

(b)

Fig.4. Scaled volume fraction distributions. (a) $\rho_1 / \rho_2 = 3$, calculation #4, (b) $\rho_1 / \rho_2 = 20$, calculation #10

For 2D numerical simulation of RM turbulent mixing, Youngs [31], figure 8, noted that vortex pairs carry small amounts of spike fluid away from the mixing zone. According to Zabusky [32] this is a more widely occurring phenomena in both 2D and 3D flows, which Zabusky referred to a “vortex projectiles” . In the late time, At=0.5 computation considered here, a single spike is observed to propagate substantially further than other flow features. This spike is visualised in Figure 5, along with the plane averaged dense fluid volume fraction, plotted on semi-logarithmic scales. An important observation is that despite the spike head being quite energetic, as discussed in more detail in Zhou et al. [33], it carries very small amounts of fluid along with it. In fact, the plane averaged volume fractions are on the order of 10^{-7} in the region influenced by that single spike alone and this has a negligible effect on the integral spike distances. Volume fraction distributions are progressing towards a self-similar state but this may not account for very small amounts of fluid at the extremes of the mixing zone. A possible more important consideration would be the impact of such spikes on multi-layered systems, where the passage of the spike through a neighbouring interface could create a substantial perturbation. Should the system then be re-shocked, the resultant growth

may be much higher than expected. There is some similarity with the behavior for the singular case, $\rho_2 = 0$. The spikes do not decelerate according to either (3) or (4), implying $\theta_b < \theta_s = 1$. However, the mass in the spike tips does not increase with time, whereas the mass in the base of the spikes increases as h_b increases. It is possible that even in this case most of the volume fraction distribution evolves towards a self-similar profile except for the very tips of the spikes.

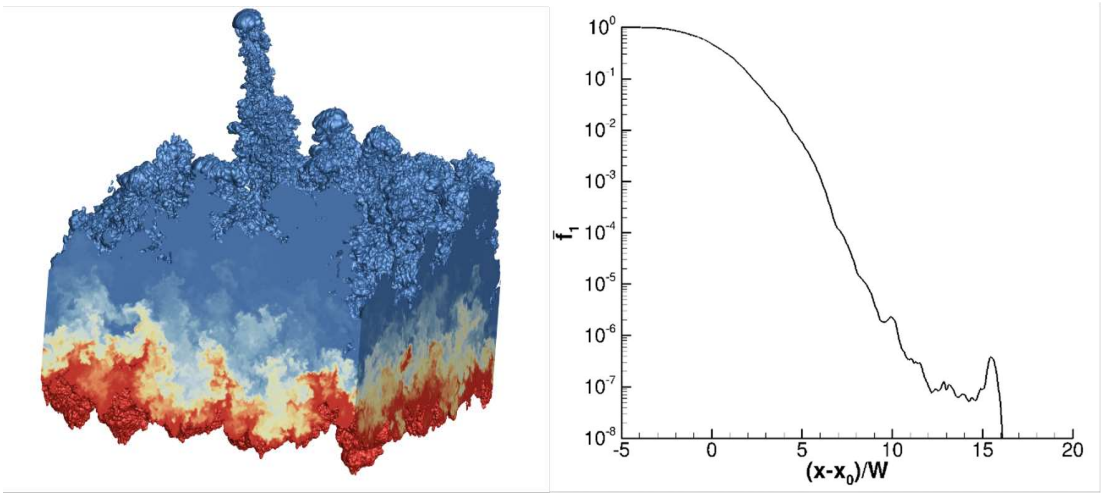

Fig.5. Visualisation of a the spike side of the longer time calculation #4, using dense fluid volume fraction of 10^{-5}, along with scaled volume fraction distribution at $W / \bar{\lambda} = 2.03$.

The simulations do not go far enough to give an accurate estimate of the asymptotic values of h_s / h_b but it is clear that volume fraction distributions for the self-similar state are not highly asymmetric. In the RM experiments of Dimonte and Schneider [7] the initial turbulence layer is created by a short period of high-acceleration RT, a different mechanism than in the simulations considered here. Thus the early time very high ratios of h_s / h_b were not observed. For $\rho_1 / \rho_2 = 2.83$ very little bubble-to-spike asymmetry was observed, with $\theta_s \simeq \theta_b$ and $h_s / h_b \simeq 1.06$ at the end of the experiment. These results are considered to be consistent with figure 3a. At much higher density ratios, h_s / h_b was increasing at the end of the experiment and $\theta_s > \theta_b$ was reported. However, at the end of the measurement range the spikes have reached the top of the tank and there are edge effects due to large bubbles and spikes in the tank corners. It is

suggested here that these factors may have influenced the results. If the data at the time when the spike is 2/3 of the distance to the top of the tank is used, then the results plotted in figure 25 of [7] indicate $h_s / h_b \sim 2.8$ for $\rho_1 / \rho_2 = 23.4$ and a similar degree of asymmetry at $\rho_1 / \rho_2 = 49.1$. Now the experiments of [7] used immiscible mixtures and at late time the spikes broke up to give a random distribution of fragments. It is expected that this would lead to a different estimate of spike distance than used here for the mixing of miscible gases. Prior to the experiments of Dimonte et al, Alon et al. [34] proposed an Atwood number dependence of θ_s based on an analysis of computational results for a multimode perturbation. Given the relatively early dimensionless time achievable with computational power in the mid-1990s those results are consistent with our early time behaviour. When all these factors are taken into account, it is concluded that there is consistency between the late time bubble-to-spike asymmetry seen in the experiments, previous simulations and the current simulations.

Use of volume fraction cut-offs ($h_b^{1\%}$ and $h_s^{1\%}$) is a commonly accepted way of defining the bubble and spike distances. Figure 6 shows plots of $h_b^{1\%} / \bar{h}_b^{(2)}$ and $h_s^{1\%} / \bar{h}_s^{(2)}$. The best value to choose for *m* is not clear. However, *m*=2 gives satisfactory results and a good approximation to $h_{b/s}^{1\%}$ is $h_{b/s} \sim 1.1\bar{h}_{b/s}^{(2)}$. Bubble and spike distances so defined will be used for the analysis of the multimode simulations (sections 7 and 8). The integral definitions of the bubble and spike widths vary much more smoothly with time than those determined by volume fraction cut-offs. As in [6], some smoothing is still required to calculate the second derivatives and thus the effective length scales given by equation (10). This is done by constructing a least-squares fit to the data for $t - \Delta t < t' < t + \Delta t$, where Δt is a suitably chosen time interval :-

$$h_{b/s} = h_{b/s}^* + V_{b/s}^* \left(t' - t\right) + \tfrac{1}{2}\dot{V}_{b/s}^* \left(t' - t\right)^2, \quad \ell_{b/s}^{eff} = -\frac{\left(V_{b/s}^*\right)^2}{\dot{V}_{b/s}^*} \qquad \text{.....(21)}$$

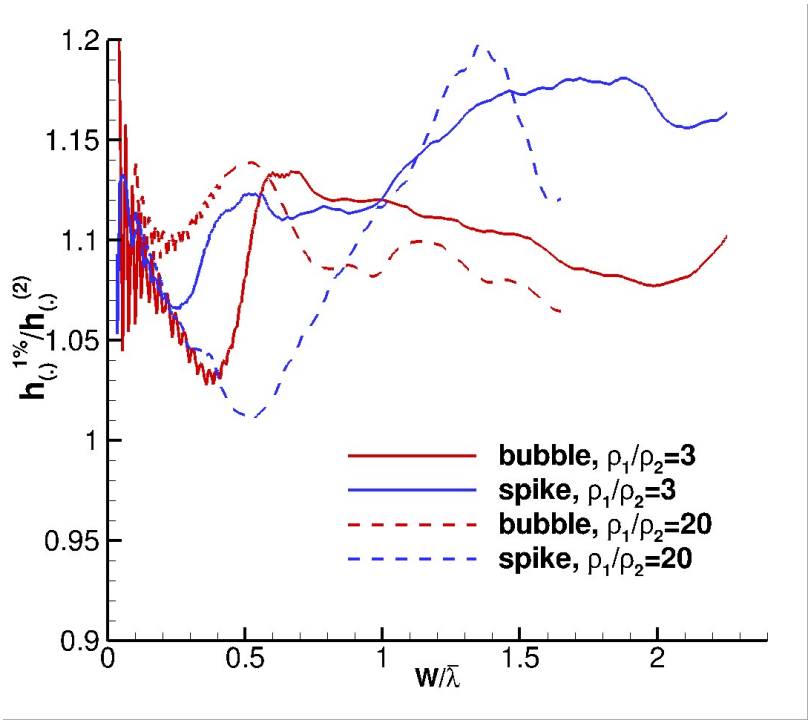

Fig.6. Plots of scaling factors for $h_b^{1\%} / \bar{h}_b^{(2)}$ and $h_s^{1\%} / \bar{h}_s^{(2)}$, calculations #4 and #10

7. Analysis of the low Atwood number data

7.1. Single-mode simulation

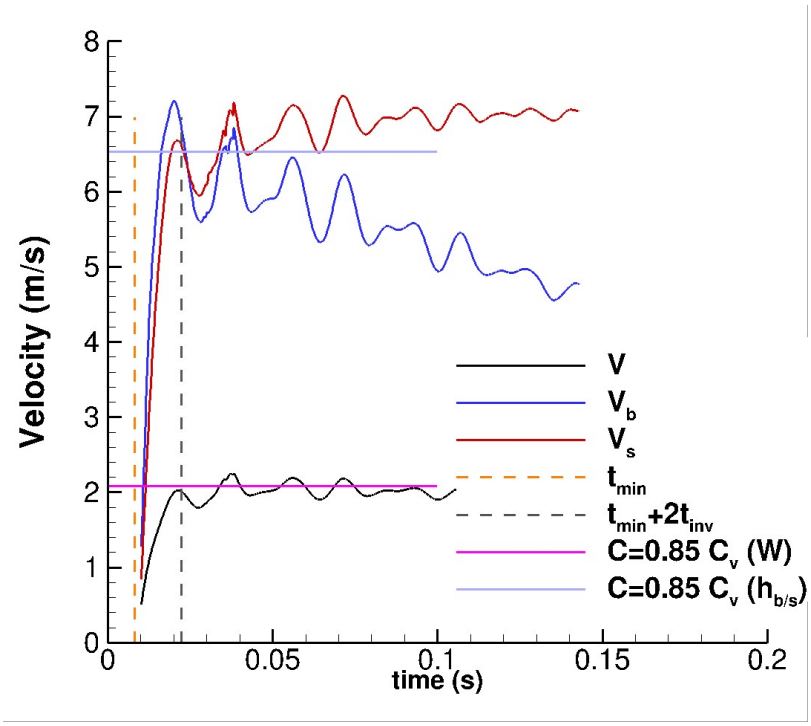

Fig 7. Mix velocities for the single mode simulation, $\rho_1 / \rho_2 = 3$

A high-resolution FLAMENCO single mode simulation has been performed with 320 meshes per wavelength. A low value of $a_0/\lambda = 0.01$ was used to ensure that behavior was in the linear regime. Three approximations were considered in [6] for the compression factor, C. According to the Richtmyer formula [21]

$\dot{a} = kC_R a_0 A^+ \Delta u$ where $C_R = 1 - \Delta u / U_s$. …(22)

According to Vandenboomgaerde et al. [23] more accurate results may be obtained with

$\dot{a} = \frac{1}{2} k \left(C_R a_0 A^+ + a_0 A \right) \Delta u = k C_V a_0 A^+ \Delta u$ …(23)

As there is little difference between A and A^+ the earlier approximation of Meyer and Blewett [22] , $\dot{a} = \frac{1}{2} k \left(C_R a_0 + a_0 \right) A^+ \Delta u$, gives similar results.

It was found that $C = 0.85 C_v = 0.576$ gave a good approximation to the peak post-shock value of dW/dt for this case. The results obtained are reproduced in figure 7 (note that there are oscillations in the post-shock velocity due to the effect of compressibility which are not accounted for in the simple impulsive model). With bubble and spike distances defined as $1.1\bar{h}_{b/s}^{(2)}$, the initial bubble and spike velocities should be a factor $1.1 \times 1.1547/0.4053 = 3.13$ higher, according to equation(19). Figure 7 shows that this is the case. For the times shown the bubble velocity decays but the spike velocity does not. As the incident shock wave travels from the heavy fluid to the light fluid here, the perturbation inverts. The amplitude is given by $a = C a_0 \left(1 - k A^+ \Delta u \, t \right)$ and the inversion time is $t_{inv} = 1/\left(k A^+ \Delta u \right)$. Peak velocities are achieved at a time $\sim 2 t_{inv}$ after the time of minimum W.

7.2. Multi-mode simulations: very early time behaviour

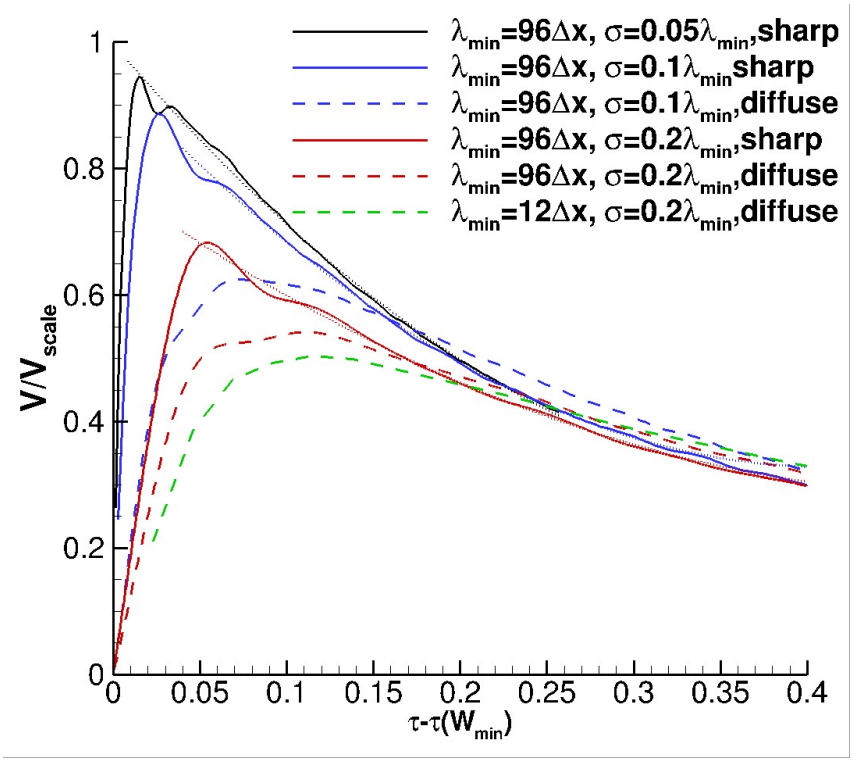

Fig8. Scaled mix velocities for $\sigma_0 = 0.05 - 0.2\bar{\lambda}$. Comparison of sharp and diffuse interfaces. Calculations #4 to #9.

As in previous papers, plots of scaled variables are shown for the multimode simulations. Lengths are scaled by $\bar{\lambda}$, velocities are scaled by $V_{scale} = V_0^{theory} = 0.564 C \sigma_0 \bar{k} \left| A^+ \Delta u \right|$ (equation 11) and the scaled time is defined by $\tau = V_{scale} t / \bar{\lambda}$.

The calculation used for the analysis of the late time behavior has a high initial amplitude, $\sigma_0 = 0.2\bar{\lambda}$, and low initial resolution, $\lambda_{\min} = 12\Delta x$. This is chosen to reduce to computation time needed to reach very large values of the scaled time, τ. In order to calculate the very early time behavior accurately results are compared with higher resolution simulations with $\lambda_{\min} = 96\Delta x$. As significant non-linear effects are expected for $\sigma_0 = 0.2\bar{\lambda}$, results are also compared with velocity plots at lower initial amplitudes, previously shown in [6]. The calculation used for the late time analysis had a diffuse

interface. Hence a comparison with sharp interface data is given. All these comparisons are shown in figure 8.

The scaled peak velocity for the sharp interface case reduces significantly as the initial perturbation amplitude is increased. Non-linear saturation effects have been investigated by Probyn et al. [24]. For single mode growth the following scaling factor is given for the peak initial velocity derived from the average of bubble and spike distances (the earlier results of Dimonte and Ramaprabhu [35] and Buttler et al. [36] give similar behavior).

$$F_{av}^{nl} = \frac{1}{\left(1+\frac{1}{2}\varepsilon^2\right)^{1/2}} \qquad \text{where } \varepsilon = ka_0 \qquad \text{.....(24)}$$

If $\varepsilon = 2\bar{k}\sigma_0 = 9.6\sigma_0 / \lambda_{\min}$ is used, this expression gives $F_{av}^{nl} = 0.95, 083, 0.59$ for $\sigma_0 = 0.05\lambda, 0.1\lambda, 0.2\bar{\lambda}$. The trend is similar to that shown in figure 8 (the correction factor for $\dot{W}$, F_W^{nl}, should be similar to F_{av}^{nl}). The diffuse interface gives a significant reduction in the peak velocity and in these cases velocities are not very sensitive to the mesh size. It is interesting to note that from about τ = 0.3 onwards all the calculations give similar values for the scaled velocity.

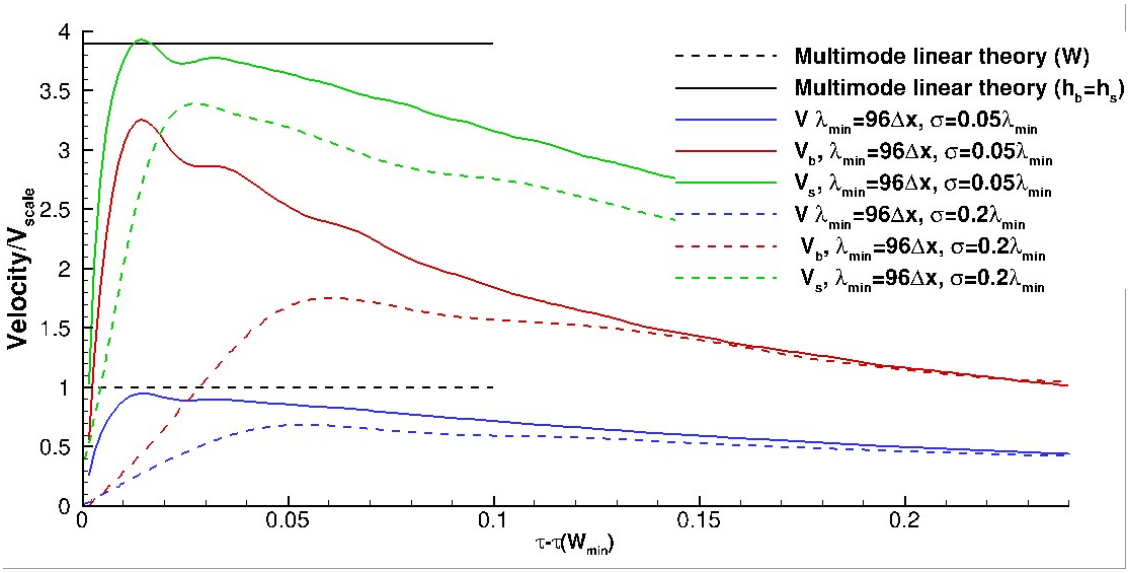

Fig9. Scaled bubble, spike and mix velocities for $\sigma_0 = 0.05, 0.2\,\lambda_{\min}$. Sharp interfaces. Calculatioins #5,8.

Figure 9 shows bubble and spike velocities for the two high-resolution simulations with $\sigma_0 = 0.05\lambda_{\min}, 0.2\,\lambda_{\min}$ and with sharp interfaces. In the absence of non-linear effects,

the scaled peak bubble and spike velocities should be the same. However, it is apparent that the peak bubble velocity is less than the peak spike velocity and that the effect is significantly greater for the higher initial amplitude. References [35,36] and Velikovich et al. [37] all show that different non-linear correction factors, F_b^{nl}, F_s^{nl}, are needed for the bubble and spike single - mode velocities. However, non-linear effects are expected to be different for the current multimode case due to the range of perturbation inversion times. The difference between t_{inv} for the shortest and longest inversion times is $\Delta t_{inv} = 1/(k_{\max} A^+ \Delta u)$. The initial decay of the single mode bubble velocity is much more rapid that that for the spike (figure 7) and has time scale $\Delta t_{vb} \sim \lambda / V_b \sim \lambda / \left(k a_0 A^+ \Delta u \right)$. For the multimode case $\Delta t_{vb} / \Delta t_{inv} \sim 1/\left(\bar{k} \sigma_0 \right)$. Hence there is an additional non-linear effect that will reduce the bubble velocity more than the spike velocity when $\bar{k}\sigma_0$ is large.

7.3. Multi-mode simulations: variation of the effective length scales

In this section the variation of ℓ^{eff}, ℓ_b^{eff} and ℓ_s^{eff}, as defined by equations (10), with mixing zone width is considered. For the integral width, *W*, variation of $\ell^{eff} / \bar{\lambda}$ with $W / \bar{\lambda}$ was given in [6] for $\sigma_0 = 0.05\lambda_{\min}$ and $0.1\lambda_{\min}$. Results for $\sigma_0 = 0.2\,\lambda_{\min}$ are now added and the plot is extended to higher values of $W / \bar{\lambda}$. The early time behavior is shown in figure 10. The solid lines show values of ℓ^{eff} derived from the raw data. The dashed lines show values of ℓ^{eff} derived from the quadratic fits to the very early time velocities shown in figure 8, which smooth over the oscillations due to compressibility. It is evident that for the sharp interface, the scaled data for $\sigma_0 = 0.2\,\lambda_{\min}$ gives very similar results to the previous data for $\sigma_0 = 0.05\lambda_{\min}$ and $0.1\lambda_{\min}$. For $W / \bar{\lambda} > 0.4$ the effect of the diffuse interface is small. All the sharp interface results $W / \bar{\lambda} < 0.5$ are well approximated by the formula used in [6]:-

$$\frac{\ell^{eff}}{\bar{\lambda}} = a - b\left\{1 - \exp\left(-c\frac{W}{\bar{\lambda}}\right)\right\} \qquad \text{.....(25)}$$

with $a = 0.3, b = 0.176, c = 8.35$

This gives the variation expected according to section 3 for the weakly non-linear and initial turbulent stages.

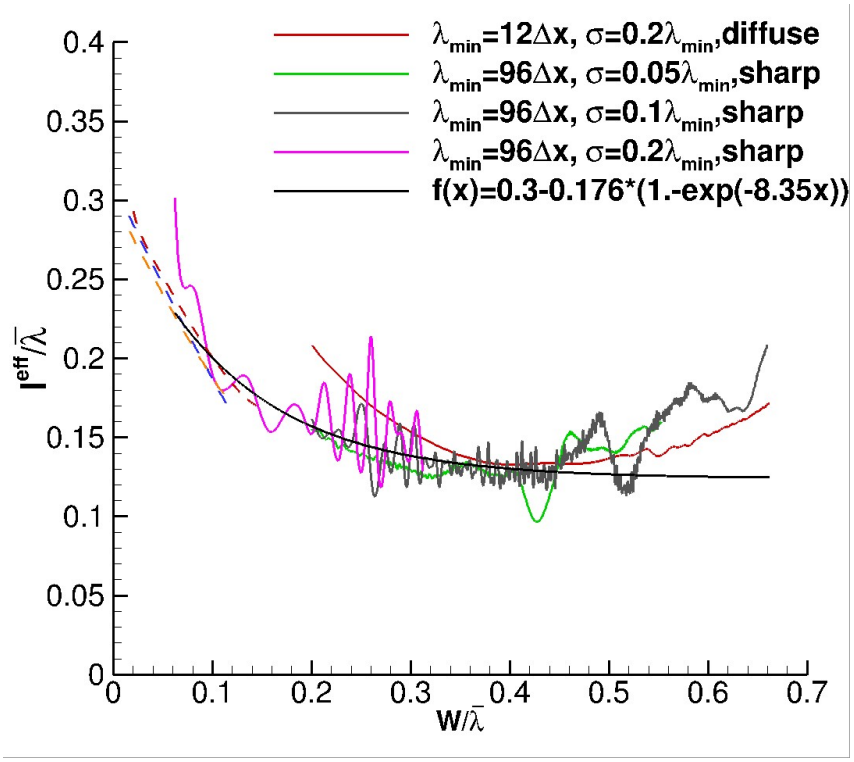

Fig.10. Early time behavior for $\ell^{eff}/\bar{\lambda}$ versus $W/\bar{\lambda}$, calculations #4,5,6,8.

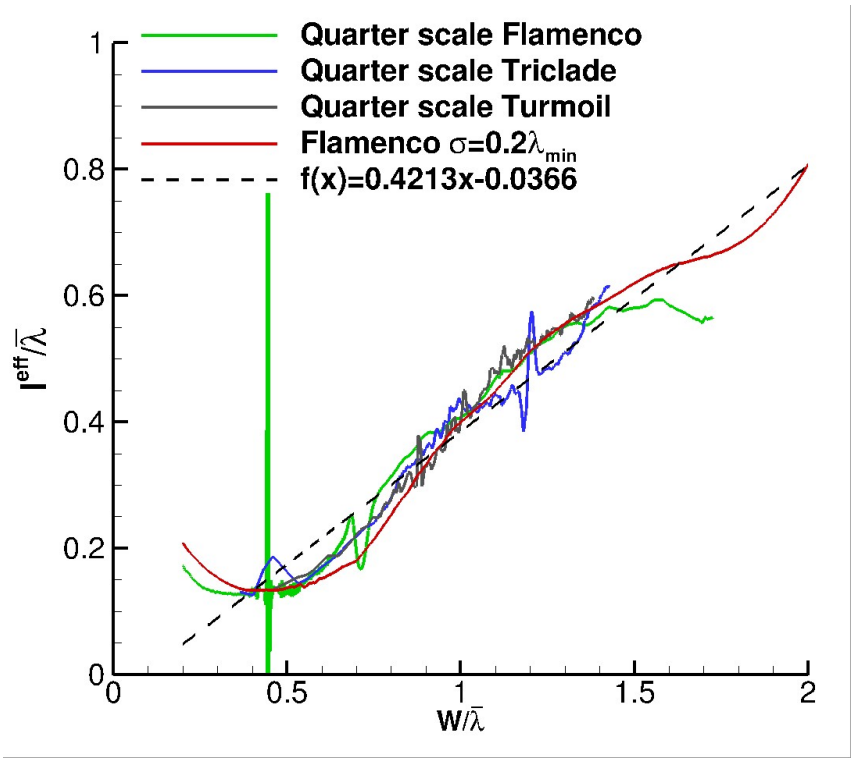

Fig.11. Late time behavior for $\ell^{eff}/\bar{\lambda}$ versus $W/\bar{\lambda}$ for calculations #1,2,3,4.

Figure 11 shows the late time variation of $\ell^{eff}/\bar{\lambda}$ with $W/\bar{\lambda}$ and compares with results given in [6]. For self-similar mixing

$$\ell^{eff} = \frac{\theta}{1-\theta} W \qquad \text{.....(26)}$$

Figure 11 does indicate an approximate linear increase at late time. However, there is a significant offset and a better late time approximation is

$$\frac{\ell^{eff}}{W} = \frac{\theta}{1-\theta}\left(\frac{W}{\bar{\lambda}} - d\right) \qquad \text{.....(27)}$$

Previous estimates of θ, [5] for example, were obtained by fitting the power law $W = A(t-t_0)^{\theta}$ to the late-stage data for W versus time. This assumes that equation (26) is valid. It now apparent that equation (27) gives a better approximation and it was proposed in [6] that the best estimate for θ is given by the slope, s_ℓ, of the line given by equation (27) , $\theta = s_\ell/(1+s_\ell)$. The linear correlation is not good as could be hoped for but it will be shown that use of equation (27) in the buoyancy-drag model gives good fits to the W versus t data. The values of θ used here are considered to be the best values for the range $\ell^{eff}/W > 0.5$ where ℓ^{eff} is increasing with time. The plots of ℓ^{eff} highlight small deviations from the θ-law model. If equation (27) is applied to a short time interval

$$\frac{1}{\theta} = 1 - \frac{\left(W - d\bar{\lambda}\right)\ddot{W}}{\left(\dot{W}\right)^2} \qquad \text{.....(28)}$$

As $d > 0$, equation (27) gives slightly higher values of θ than equation (26).

The previous FLAMENCO results showed some levelling off at late time and this was attributed to the effects of the computational domain boundaries. The present extended time calculation gives similar results to the previous simulations and shows ℓ^{eff} continuing to increase at late time. For the extended time FLAMENCO calculation $s_\ell = 0.421$ and $\theta = 0.30$. This is slightly less than the previous estimates of $\theta = 0.31$ to 0.37 derived in [6] from the FLAMENCO, TRICLADE and TURMOIL data. There is significant uncertainty in estimating the late time slope, s_ℓ, and all results are likely to be affected by reflections from the boundaries. Hence all the values of θ are considered to be consistent the theoretical value of 1/3 given by Elbaz and Shvarts [17] for the narrowband initial perturbation case.

In the version of the buoyancy-drag model used here the length scales in the bubble and spike equations are both related to the bubble distance. Hence both effective length scales are plotted against $h_b / \bar{\lambda}$. Figure 12 shows the early time behavior. As for the effective length scale for *W,* figure 10, quadratic fits to the very early time velocities are used at $h_b / \bar{\lambda} < 0.4$. The sharp interface high-resolution results are used for $0.4 < h_b / \bar{\lambda} < 0.7$ and data from the late time calculation with $\lambda_{\min} = 12\Delta x$ is used for $h_b / \bar{\lambda} > 0.7$. At the very early time, data is available for both $\sigma_0 = 0.05\lambda_{\min}$ and $0.2\,\lambda_{\min}$ and in this case there is some variation with the initial perturbation amplitude. The results show that $\ell_s^{eff} > \ell_b^{eff}$ at early time with ℓ_b^{eff} and ℓ_s^{eff} dropping to similar values at $h_b / \bar{\lambda} \sim 2$. The behavior is more complex than for the integral width, figure 10, and difficult to represent accurately. The same exponential form, equation (25) will be used with coefficients optimised to fit the early time bubble and spike data. The approximations that will be used in the next subsection have been added to figure 12.

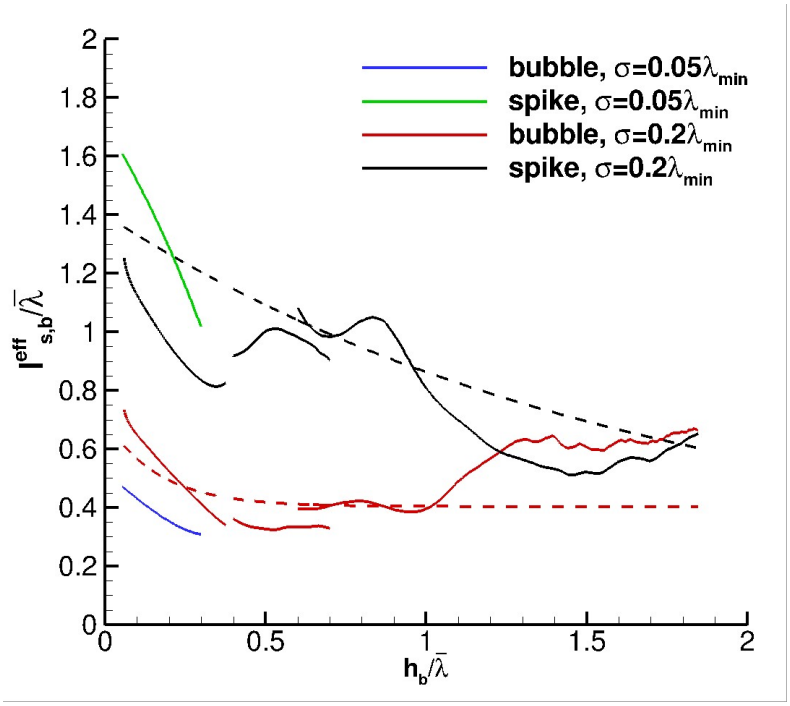

Fig.12. Early time behavior for $\ell_b^{eff} / \bar{\lambda}$ and $\ell_b^{eff} / \bar{\lambda}$ versus $h_b / \bar{\lambda}$, data from calculations #4,5,8

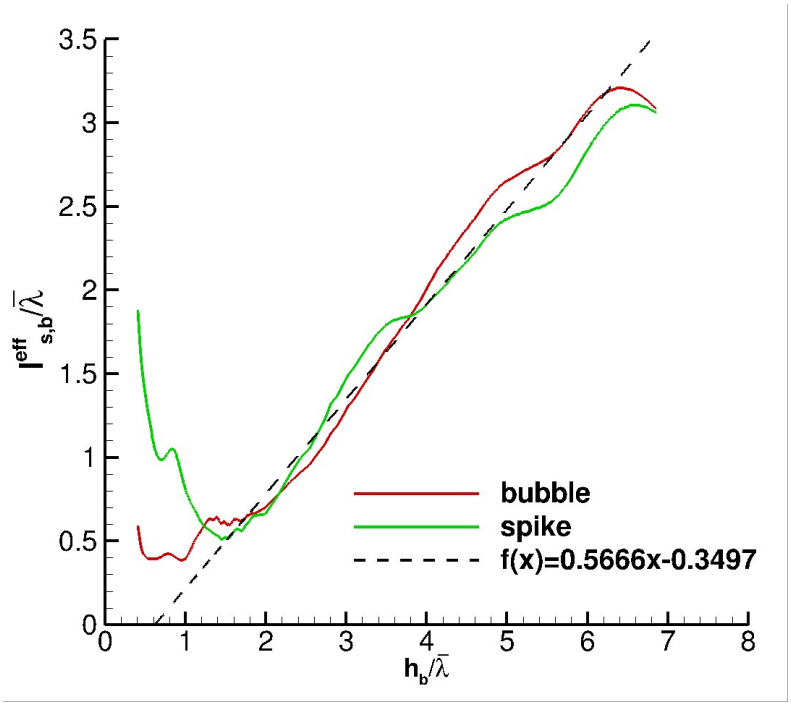

Fig.13. Late time behavior for $\ell_b^{eff}/\bar{\lambda}$ and $\ell_s^{eff}/\bar{\lambda}$ versus $h_b/\bar{\lambda}$, calculation #4.

The late time behavior of the bubble and spike length scales is shown in figure 13. This shows a linear increase in the length scales for $h_b/\bar{\lambda} > 2$. The dotted curve shows a linear fit to the data for ℓ_b^{eff}. It appears that the influence of the boundaries affects the results at the very end of the simulation. The value of θ may also be derived from the slope of the plot of $\ell_b^{eff}/\bar{\lambda}$ versus $h_b/\bar{\lambda}$. The result obtained is $\theta = 0.566/1.566 = 0.36$. This is higher than the value of θ=0.30 derived from the data for *W*. The results suggest that an intermediate value corresponding to the theoretical value of θ= 1/3 is appropriate for modelling purposes. At very late time $\ell_s^{eff}/\ell_b^{eff}$ should approach *R*, the self-similar value of h_s/h_b and this should be slightly greater than unity. It is not possible to obtain a good estimate of *R* from figure 13, other than to say that it is close to unity.

7.4. Buoyancy-Drag modelling

The buoyancy-drag model with corrections for initial conditions is now compared to the iLES data for the case $\sigma_0 = 0.2\,\lambda_{min}$. The model assumes a sharp initial interface. Hence at early time the comparison is made with the high-resolution sharp interface data as well as the diffuse interface data with $\lambda_{min} = 12\Delta x$.

The modified model is as follows

$$\frac{dW}{dt}=V,\ \frac{dV}{dt}=-\frac{V^2}{\ell^{eff}};\quad \frac{dh_b}{dt}=V_b,\ \frac{dV_b}{dt}=-\frac{V_b^2}{\ell_b^{eff}};\quad \frac{dh_s}{dt}=V_s,\ \frac{dV_s}{dt}=-\frac{V_s^2}{\ell_s^{eff}} \qquad ...(29)$$

It is assumed that θ=1/3 for bubbles, spikes and the integral width. The effective length scales are based on the analysis given in the previous subsections and are approximated by

$$\frac{\ell^{eff}}{\bar{\lambda}}=\max\left\{a-b\left(1-e^{-c\frac{W}{\bar{\lambda}}}\right),\frac{\theta}{1-\theta}\left(\frac{W}{\bar{\lambda}}-d\right)\right\}$$

with $a=0.3, b=0.176, c=8.35, d=0.237$

$$\frac{\ell_b^{eff}}{\bar{\lambda}}=\max\left\{a_b-b_b\left(1-e^{-c_b\frac{h_b}{\bar{\lambda}}}\right),\frac{\theta}{1-\theta}\left(\frac{h_b}{\bar{\lambda}}-d_b\right)\right\} \qquad ....(30)$$

with $a_b=0.7, b_b=0.297,\ c_b=6.0,\ d_b=0.293$

$$\frac{\ell_s^{eff}}{\bar{\lambda}}=\max\left\{a_s-b_s\left(1-e^{-c_s\frac{h_b}{\bar{\lambda}}}\right),\frac{\theta}{1-\theta}R\left(\frac{h_b}{\bar{\lambda}}-d_s\right)\right\}$$

with $a_s=1.4, b_s=1.19,\ c_s=0.6,\ d_s=0.60,\ R=1.1$

For modelling the integral width, values of the parameters *a*, *b*, *c*, *d* are the same as those used in [6] for $\sigma_0=0.1\lambda_{\min}$. The parameters $a_{b/s}, b_{b/s}, c_{b/s}$ are found by optimising the fit to the early stage values of h_b, h_s and the parameters d_b, d_s and *R* (the late-stage self-similar value of h_s/h_b) are found by optimizing the fit to the late-stage values of h_b, h_s .

The initial conditions also need to be specified. Results are insensitive to the values chosen for the initial mix widths as initial decay of velocity is determined by $\bar{\lambda}$ not by the initial amplitudes. The values used are $W_0=0.5642C\sigma_0$ and $h_b^0=h_s^0=1.1\times 2.0C\sigma_0$ where *C* is the amplitude compression factor and the factor of 1.1 accounts for the difference between the 1% threshold and the integral definitions of h_b, h_s as detailed in section 6. The remaining numerical factors come from equation (20). The buoyancy-drag model does not aim to represent the perturbation inversion process and starts just after $t=t_{\min}$ when $W_{iLES}=W_0$. The initial velocities are based on the linear multimode impulsive theory with a correction for compressibility, *C* , and corrections for non-linearity. It is apparent from previous studies, [35-37] that the

corrections for non-linearity should be different for bubbles and spikes. The initial velocities are then

$$V_0 = 0.5642 C\bar{k}\sigma_0 \Delta u \times F_W^{nl}$$
$$V_{b0} = 1.1\times 2.0\, C\bar{k}\sigma_0 \Delta u \times F_b^{nl} \qquad \text{...(31)}$$
$$V_{s0} = 1.1\times 2.0\, C\bar{k}\sigma_0 \Delta u \times F_s^{nl}$$

The compression factor is determined from the single mode simulation, section 7.1, and the value used is $C = 0.85 C_v = 0.576$. The non-linearity factors, which should be unity at very low perturbation amplitudes, are found by matching the initial growth of the mixing zone. It would be desirable to investigate how these factors vary with σ_0 but this is beyond the scope of the present paper. It should be noted that the peak bubble velocity occurs at a slightly later time that the peak spike velocity (figure 9). It is not considered necessary to include this effect in the model but it may have some influence on the way the non-linear factors are determined here.

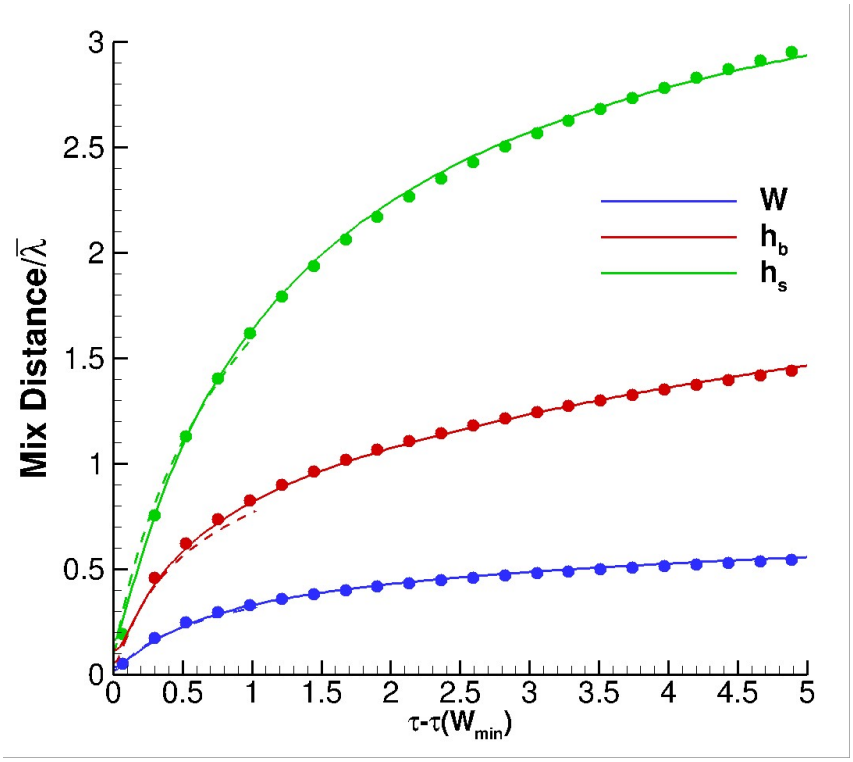

(a)

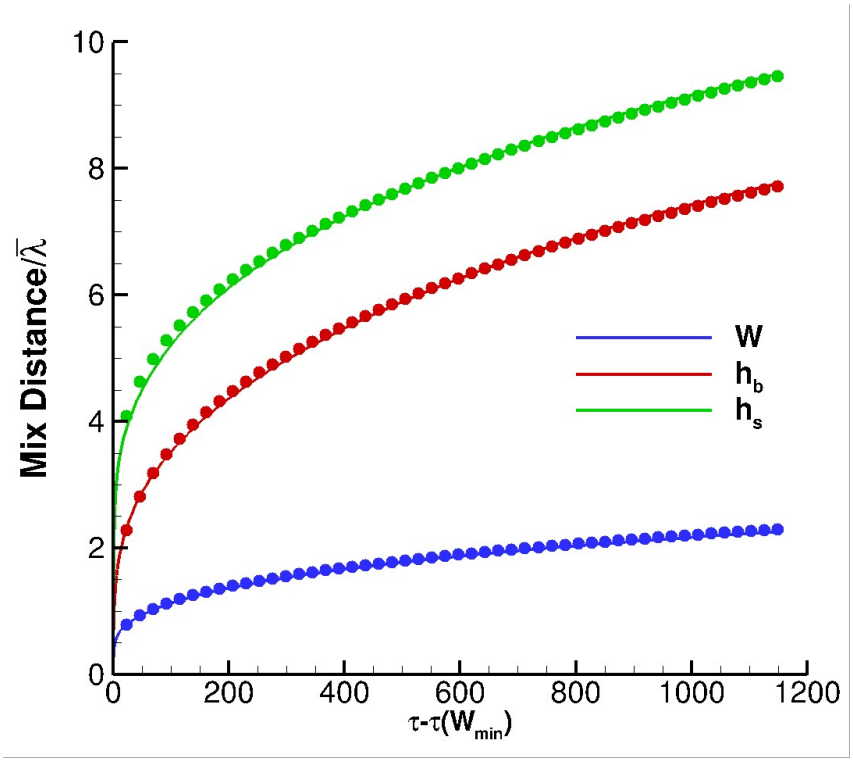

(b)

Fig.14 Application of the Buoyancy-Drag model to the FLAMENCO data for $\sigma_0 = 0.2\,\lambda_{\min}$ (a) early time, (b) late time. Solid lines: $\lambda_{\min} = 12\Delta x$, diffuse interface, calculation #4. Dashed lines: $\lambda_{\min} = 96\Delta x$, sharp interface, calculation #8. Circles: buoyancy-drag model

Comparison of the buoyancy-drag model with the iLES data is shown in figures 14a (early time) and 14b (late time). At very early time the iLES data for the $\lambda_{\min} = 96\Delta x$, sharp interface case is added to the plot in figure 14a. This differs only slightly from the data for $\lambda_{\min} = 12\Delta x$ which is used for comparison with the model at later times. The data for the integral mix width, *W*, is well matched using same parameters as for the lower amplitude case, $\sigma_0 = 0.1\lambda_{\min}$ The only difference in the modelling is that $F_W^{nl} = 0.85$ for $\sigma_0 = 0.1\lambda_{\min}$ whereas $F_W^{nl} = 0.7$ for $\sigma_0 = 0.2\lambda_{\min}$. For the bubble and spike data $F_b^{nl} = 0.40$, $F_s^{nl} = 0.80$, $d_b = 0.27, d_s = 0.65$, $R = 1.1$. Figure 15 shows plots of the spike to bubble ratio, h_s / h_b from figure 3a versus $h_b / \bar{\lambda}$. The buoyancy-drag model gives a good representation of the behavior. The reduction in h_s / h_b towards the end of the calculation is well matched and this suggests little late-time asymmetry with $h_s / h_b = R \sim 1.1$ for the final self-similar state. As previously noted, the RM, impulsive acceleration experiments at $\rho_1 / \rho_2 = 2.83$ of Dimonte and Schneider [7] giving

$h_s / h_b \sim 1.06$. The estimates of *R* are not precise and the agreement between model and experiment is considered satisfactory.

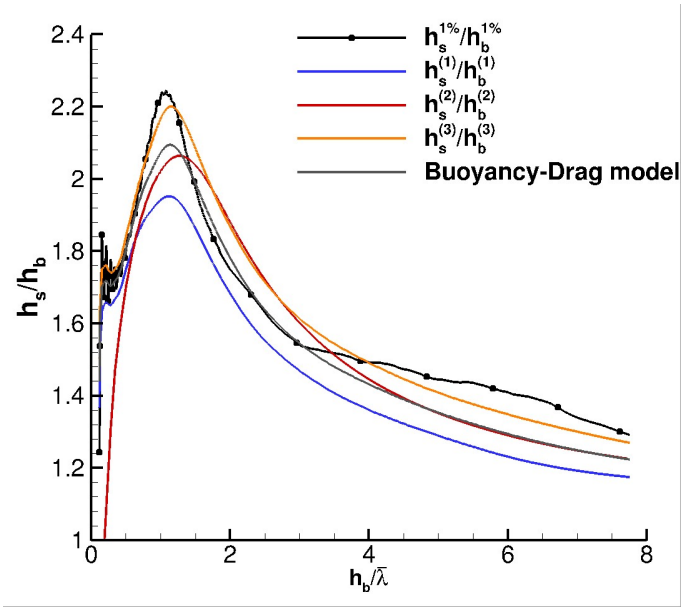

Fig.15 The spike to bubble ratio, h_s / h_b. Comparison of buoyancy-drag model with the iLES data, calculation #4.

8. Analysis of high Atwood number data

8.1. Single-mode simulations

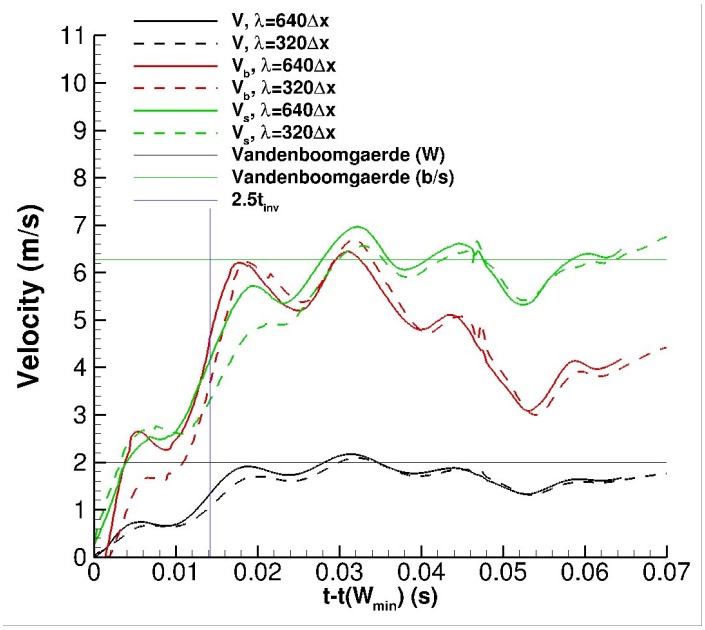

Fig16. Mix velocities for the single mode simulation, $\rho_1 / \rho_2 = 20$

Single mode calculations have been performed with 320 and 640 meshes per wavelength and $a_0 / \lambda = 0.01$. Integral width, bubble and spike velocities are shown in figure 16. In this case the Vandenboomgaerde et.al formula, without any adjustment , gives a good approximation to the peak velocities. As for the lower Atwood number case, the linear theory velocities shown in figure 16 assume $\dot{W} = 0.4053\dot{a}$ and $\dot{h}_b = \dot{h}_s = 1.1\dot{h}_b^{(2)} = 1.270\dot{a}$. Unlike the lower Atwood number case there are low initial peaks in the velocity plots soon after t_{min}, the time of minimum *W*. The first major velocity peaks occur at about 2 ½ times the perturbation inversion time, $t_{inv} = 1/\left(kA^{+}\Delta u\right)$. This is slightly longer that for the lower Atwood number case and implies that for the multimode case the non-linear effect of the range of perturbation times may be greater.

8.2. Multi-mode simulations: very early time behaviour

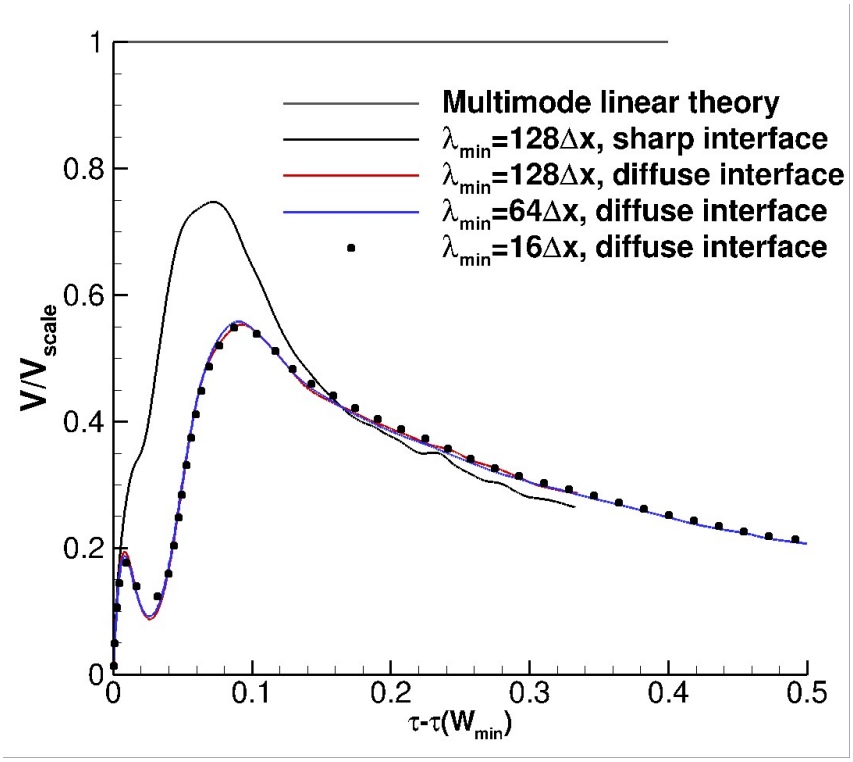

Fig 17. Scaled mix velocities V / V_{scale}. Comparison of sharp and diffuse interfaces. Calculations #10,11,12,13

Figure 17 shows plots of the integral with mix velocities scaled by the velocity given by the multimode linear theory, equation(11), using the Vandenboomgaerde

compressibility correction. As for the lower Atwood number case, the scaled time is $\tau = V_{scale} t / \bar{\lambda}$. For the sharp interface calculation the peak mix velocity is about 75% of that given by the linear theory. It is reasonable to attribute this to non-linear saturation, which may be greater than for the lower Atwood number case. The effect of the diffuse interface is significant and insensitive to the mesh resolution. Even with $\lambda_{\min} = 16\Delta x$, used in the simulation for the late stage analysis, the results are reasonably accurate. Beyond $\tau - \tau_{\min} \sim 0.2$, the mix velocity decays at a similar rate in both the sharp and diffuse interface cases. It is interesting to note that there is a small but pronounced initial peak in the velocity plot for the diffuse interface case which may be related to the initial bumps seen in the single mode velocity, figure 16. This has yet to explained and may warrant further investigation.

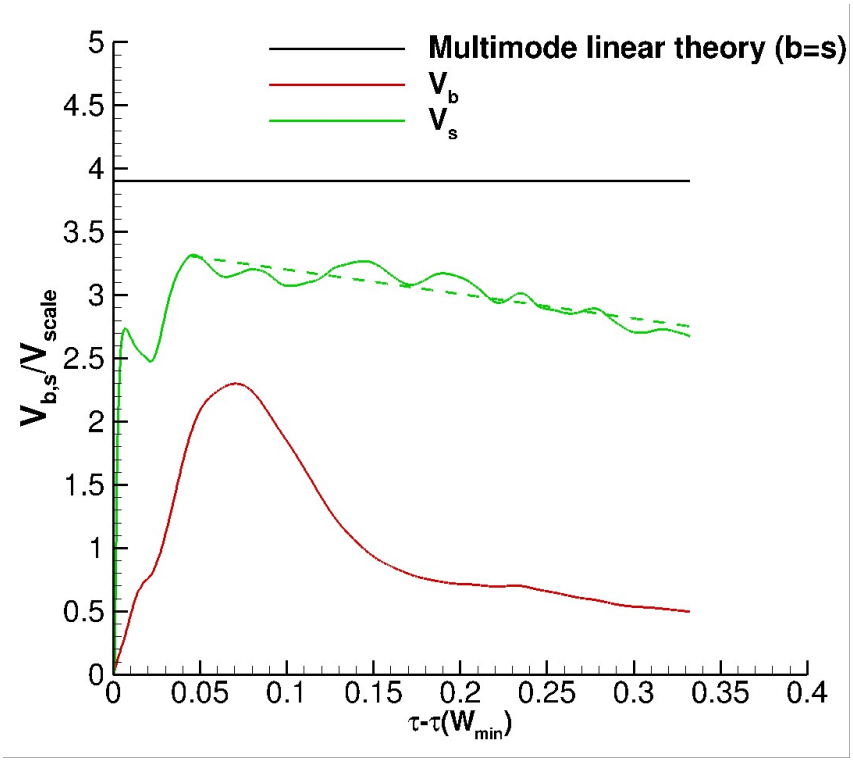

Fig.18 Scaled bubble and spike velocities. $\lambda_{\min} = 128\Delta x$, sharp interface, calculation #11.

Figure 18 shows plots for the bubble and spike velocities, defined as $\dot{h}_{b/s} = 1.1\dot{h}^{(2)}_{b/s}$, for the sharp interface case. The scaling factors for the Gaussian distribution, equation (20), indicate that the bubble and spike velocities given by the linear theory should be $3.9V_{scale}$. The peak spike velocity is about 85% of that indicated be the linear theory. The peak bubble velocity is significantly lower. As for the low Atwood number case, the

difference is attributed to a larger non-linear correction for the bubble velocity than for the spike velocity.

8.3. Multi-mode simulations: variation of the effective length scales

As for the lower Atwood number case, section 7.4 , the Buoyancy-Drag model will assume a sharp interface. Values of the effective length scales, ℓ^{eff}, ℓ_b^{eff} and ℓ_s^{eff}, as defined by equation (10), will be calculated using data from the sharp interface ($\lambda_{min} = 128\Delta x$) calculation at early time, $\tau - \tau_{min} < 0.3$, and for diffuse interface ($\lambda_{min} = 16\Delta x$) calculation beyond that time and up to $\tau = 340$, where results should not be greatly affected by the lower resolution or by the interface diffuseness. Figure 19 shows the early time behaviour for ℓ^{eff} and compares results with the best fit used for ℓ^{eff} at the the lower Atwood number case. For the sharp interface, $\lambda_{min} = 128\Delta x$, calculation only results for $\tau - \tau_{min} > 0.1$, beyond the peak in $\dot{W}$ where the mix velocity is decaying, are used. There are some fluctuations due to the fact that the decay of $\dot{W}$ (figure 17) is not entirely smooth. Unlike the lower Atwood number case, the initial reduction in ℓ^{eff} as W increases is not seen and a gradual linear increase is more appropriate. The overall level is, however, similar to that found at the lower Atwood number.

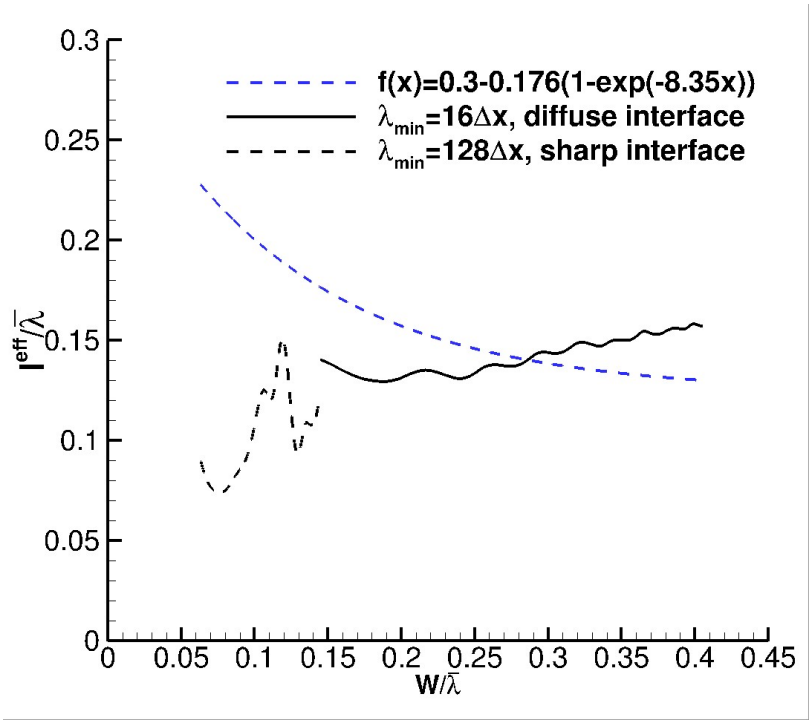

Fig.19. Early time behavior for $\ell^{eff} / \bar{\lambda}$ versus $W / \bar{\lambda}$, calculations #10,11

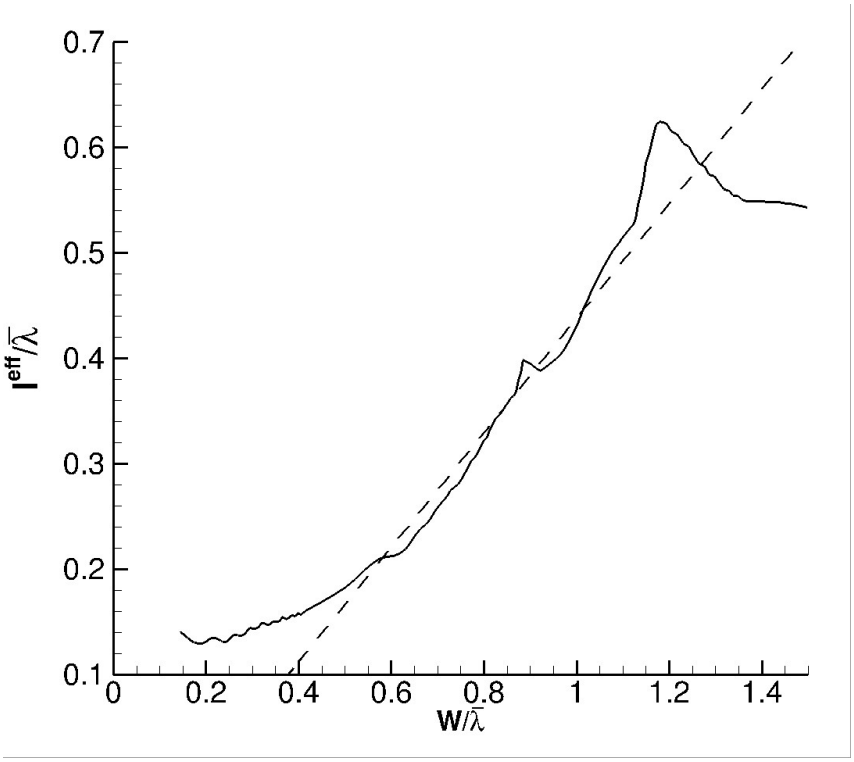

Fig.20. Late time behavior for $\ell^{eff}/\bar{\lambda}$ versus $W/\bar{\lambda}$, calculation #10.

Figure 20 shows the late time behaviour of ℓ^{eff}. There is an approximately linear increase with W from about $W/\bar{\lambda} = 0.6$ onwards and the slope of the line $s_\ell = 0.543$ indicates $\theta = 0.543/1.543 = 0.35$. Reflections from the computation domain boundaries still appear to influence the results as indicated by the reduction in ℓ^{eff} at the end of the simulation. This estimate of θ is considered to be subject to significant uncertainty.

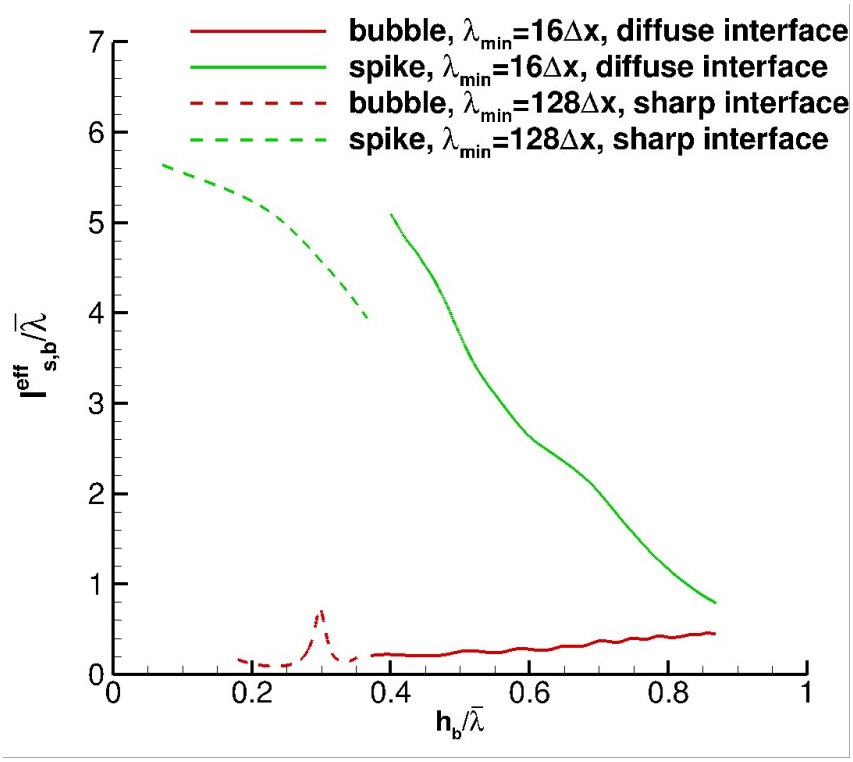

Fig.21. Early time behavior for $\ell_b^{eff}/\bar{\lambda}$ and $\ell_s^{eff}/\bar{\lambda}$ versus $h_b/\bar{\lambda}$, calculations #10,11.

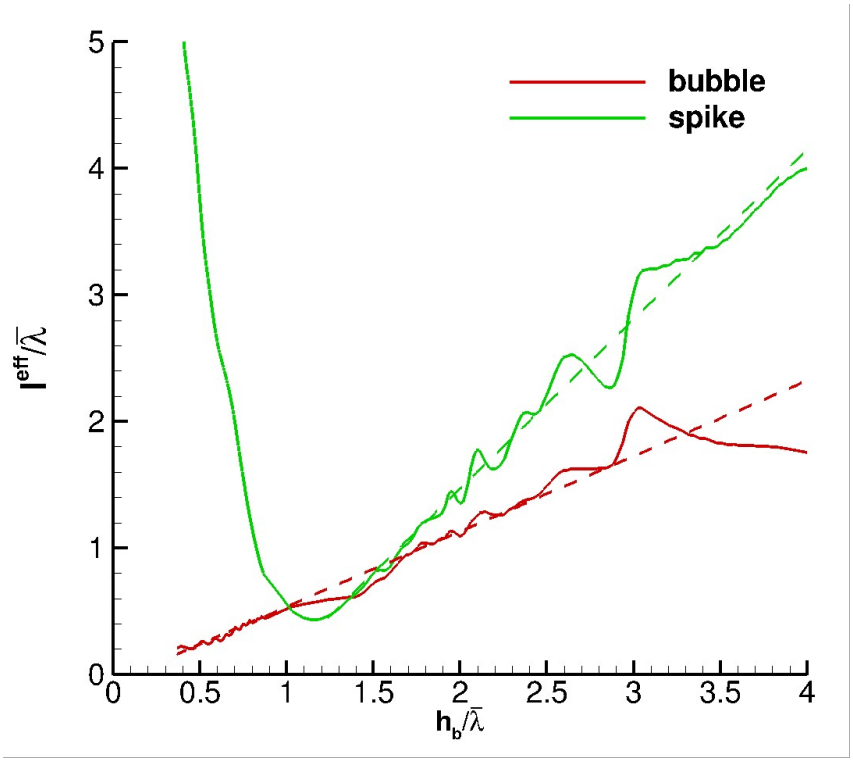

Fig.22. Late time behavior for $\ell_b^{eff}/\bar{\lambda}$ and $\ell_s^{eff}/\bar{\lambda}$ versus $h_b/\bar{\lambda}$: $\lambda_{\min} = 16\Delta x$, diffuse interface, calculation #10.

The behavior of the bubble and spike effective length scales, ℓ_b^{eff} and ℓ_s^{eff}, is shown in figure 21 (early time) and figure 22 (late time). As for the integral width, data from the $\lambda_{\min} = 128\Delta x$, sharp interface calculation is used at very early time. As there are oscillations in the spike velocity at very early time, the linear fit shown in figure 18 is used to calculate ℓ_s^{eff} here. It apparent that at the higher Atwood number there is a major difference between the behavior of the spike and the bubbles at early time with ℓ_s^{eff} exceeding ℓ_b^{eff} by a large factor. There is clearly little dissipation on the spike side at early time. As time proceeds dissipation on the spike side builds up and at $h_b / \bar{\lambda} \sim 1$, $\ell_s^{eff} \sim \ell_b^{eff}$. From then on both ℓ_b^{eff} and ℓ_s^{eff} show an approximate linear increase with h_b. For the bubble length scale, the average late-time slope ($h_b / \bar{\lambda} = 1.5 \text{ to} 3.5$) is 0.65 and this implies θ=0.65/1.65=0.39 and as for the lower Atwood number case, this is higher that the value indicated by the data for *W*. The difference in the estimates of θ is attributed to the lack of a fully self-similar range (for $h_b / \bar{\lambda} = 1.5 \text{ to} 3.5$, h_s / h_b drops from 3.6 to 2.3). Unlike the results for the lower Atwood number case, figure 13, ℓ_s^{eff} clearly exceeds ℓ_b^{eff} at late time. The late-time slope of the plot for ℓ_s^{eff} / h_b is 1.36. If $\theta_b = \theta_s$ is assumed as implied by figure 3(b), this suggests that the late-time, self-similar value of h_s / h_b should, according to equation (9), be ~1.36/0.65=2.1.

8.4. Buoyancy-Drag modelling

The buoyancy-drag model (29) is now applied to the high Atwood number data. The model coefficients are optimised to fit the mix distance data for the $\lambda_{\min} = 16\Delta x$ iLES simulation. Results are also compared with the higher resolution $\lambda_{\min} = 128\Delta x$ at very early time. As for the lower Atwood number case, the model is initialized with $W_0 = 0.5642 C\sigma_0$ and $h_b^0 = h_s^0 = 1.1 \times 2.0 C\sigma_0$ just after $t = t_{\min}$ when $W_{iLES} = W_0$. For the initial velocities, non-linear correction factors, $F_W^{nl} = 0.80, F_b^{nl} = 0.70, F_s^{nl} = 0.80$ are used to match the very early time growth, shown in figures (23a) and (24a). For the integral width and the bubble distance this is similar for two mesh resolutions. However, the

higher resolution, sharp interface iLES, gives a slightly higher initial spike velocity and this implies a non-linear correction factor, F_s^{nl} , closer to unity than used here.

The early time behavior of ℓ^{eff} is somewhat different to that for the lower Atwood case, see figure 19, and shows ℓ^{eff} gradually increasing with *W*. A different approximation is used:

$$\frac{\ell^{eff}}{\bar{\lambda}} = \max\left\{a + b\frac{W}{\bar{\lambda}}, \frac{\theta}{1-\theta}\left(\frac{W}{\bar{\lambda}} - d\right)\right\} \qquad \ldots(32)$$

For the bubbles and spikes, the behavior at the two Atwood numbers is clearly different. In order to find the best fit to the data for h_b and h_s, the functional forms used are guided by the plots shown figures 21 and 22. The approximations used are:-

$$\frac{\ell_b^{eff}}{\bar{\lambda}} = \max\left\{a_b + b_b\frac{h_b}{\bar{\lambda}}, \frac{\theta}{1-\theta}\left(\frac{h_b}{\bar{\lambda}} - d_b\right)\right\}$$
$$\frac{\ell_s^{eff}}{\bar{\lambda}} = \max\left\{a_s - b_s\frac{h_b}{\bar{\lambda}}, 0.4, \frac{\theta}{1-\theta}R\left(\frac{h_b}{\bar{\lambda}} - d_s\right)\right\} \qquad \ldots.(33)$$

In the expression for $\ell_s^{eff}/\bar{\lambda}$, the minimum value of 0.4 is indicated by figure 21 and ensures positive values.

The parameters *a* and *b* are first optimized to fit the data for $W/\bar{\lambda} < 0.6$ and the parameters a_b and b_b are chosen to optimise the fits to $h_b/\bar{\lambda}$ for the range $0.2 < h_b/\bar{\lambda} < 0.8$. The estimate of θ=0.35 and 0.39 from the slopes of the line in figures 20 and 22 is subject to significant uncertainty and choosing θ and d or d_b to optimize the fit to the late time data was considered a possible alternative. It should be noted that this gives a different result to fitting the late time data with W or $h_b = A(t - t_0)^{\theta}$,as used in earlier papers [5,8] , as this functional form assumes $d = d_b = 0$. Optimizing the fit to the data for W gave θ=0.33. It is perhaps fortuitous that the value found for θ is so close to 1/3. Optimizing the fit to the data for h_b gave a higher value of θ = 0.37. It is apparent that there is significant uncertainty in choosing the best estimate of θ. It was found that with two parameters to vary, θ and d or d_b , a very good fit to the data could be found for a range of values of θ and a common value of θ=0.35 has been used here. Finally, the fit

to the spike data, with this value of θ, is optimized by varying a_s , b_s, d_s and R, the self-similar value of h_s / h_b . The parameter values finally chosen for θ=0.35 are:

Integral width	$a = 0.1158,\ b = 0.10,\quad d = 0.189$
Bubble	$a_b = 0.105,\ b_b = 0.3175, d_b = 0.061$
Spike	$a_s = 6.44,\quad b_s = 6.41,\quad d_s = 0.649,\ R = 1.9$

Figures 23, 24, and 25 show that the optimized model gives an excellent fit to all the data. According to the model results, the estimate of the self-similar value of $h_s / h_b = h_s^{(2)} / h_b^{(2)}$ is 1.9. There is no need to doubt the assumption made here that $\theta_b = \theta_s$. As h_s / h_b is reducing rapidly towards the end of the simulation, there is not a wide range of near self-similar behavior and this implies that simulations need to be carried to a much later stage for an accurate estimate of θ.

Results for the uncorrected buoyancy drag model, $\ell^{eff} = W / C_D = W\theta / (1-\theta)$, using the same initial conditions have been added to figure 23. The uncorrected model significantly underestimates the growth of the mixing zone width.

It was noted in the previous sub-section that at early time the overall values of $\ell^{eff} / \bar{\lambda}$ are similar for the two Atwood numbers. Moreover, the chosen values of θ are similar. Hence figure 23 also shows the result of using the low Atwood formula (with θ=1/3) for the high Atwood number case. The fit to the data is not as accurate as for the optimized fit but is still satisfactory, especially at late time. It seems likely that the lower Atwood model for $\ell^{eff} / \bar{\lambda}$ will be applicable to a wide range of initial amplitudes and density ratios. However, further calculations are needed to confirm this. On the other hand, the early time behavior of $\ell_{b/s}^{eff} / \bar{\lambda}$ is so different for the two Atwood numbers that, without further investigation and additional iLES, is it not practical to recommend a simple prescription for the bubble and spike equations valid for a range of density ratios.

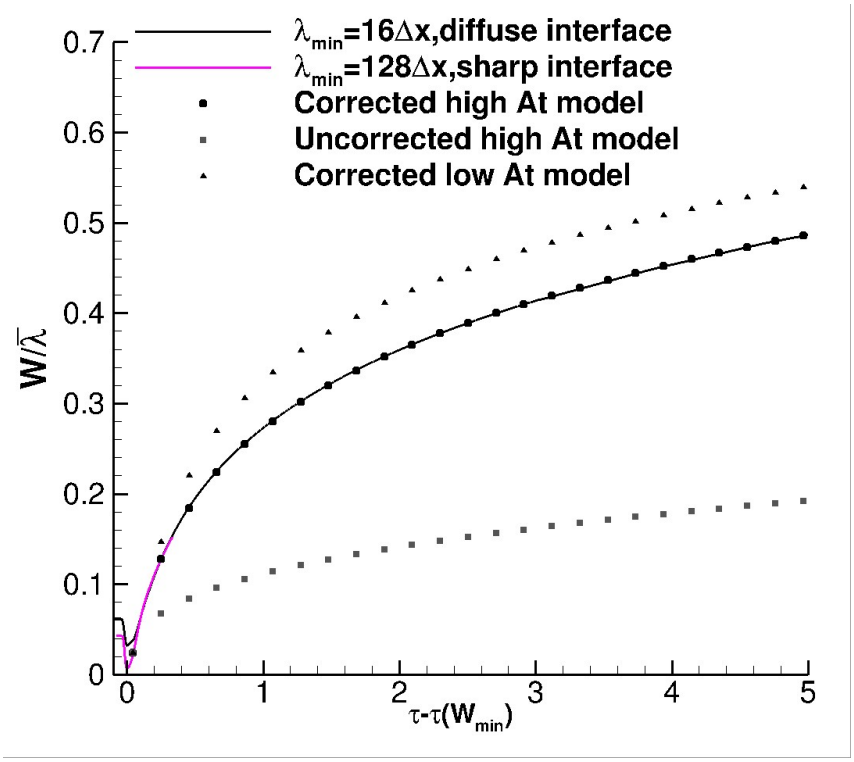

(a)

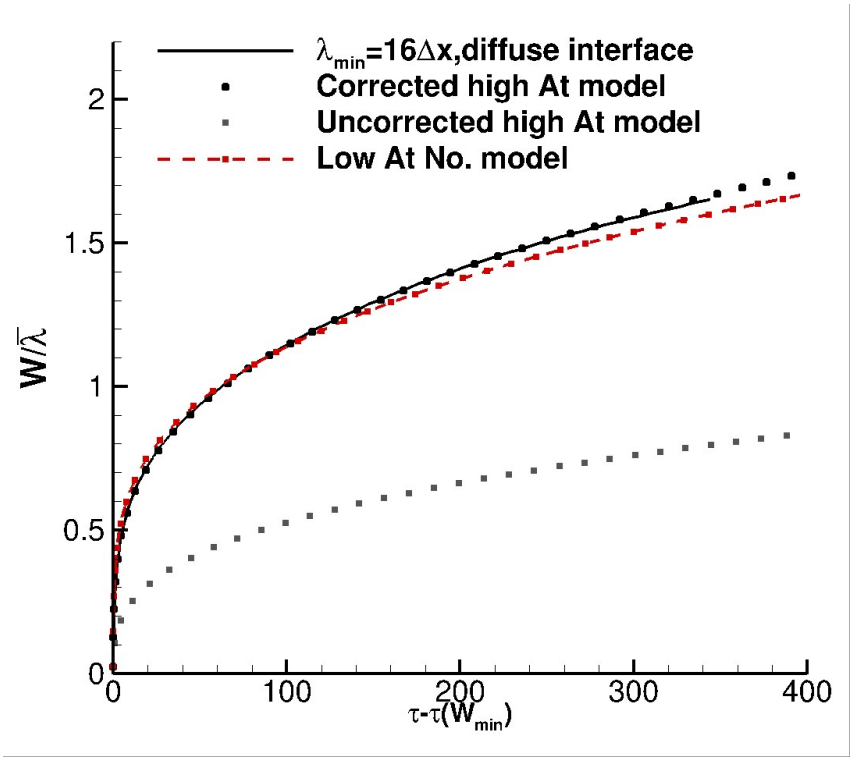

(b)

Fig.23 Application of the Buoyancy-Drag model to the FLAMENCO data, calculations #10,11 . Integral mix widths for the high Atwood number case. (a) early time, (b) late time. Solid lines: iLES data, calculations #10,11. Dots: optimised buoyancy-drag model

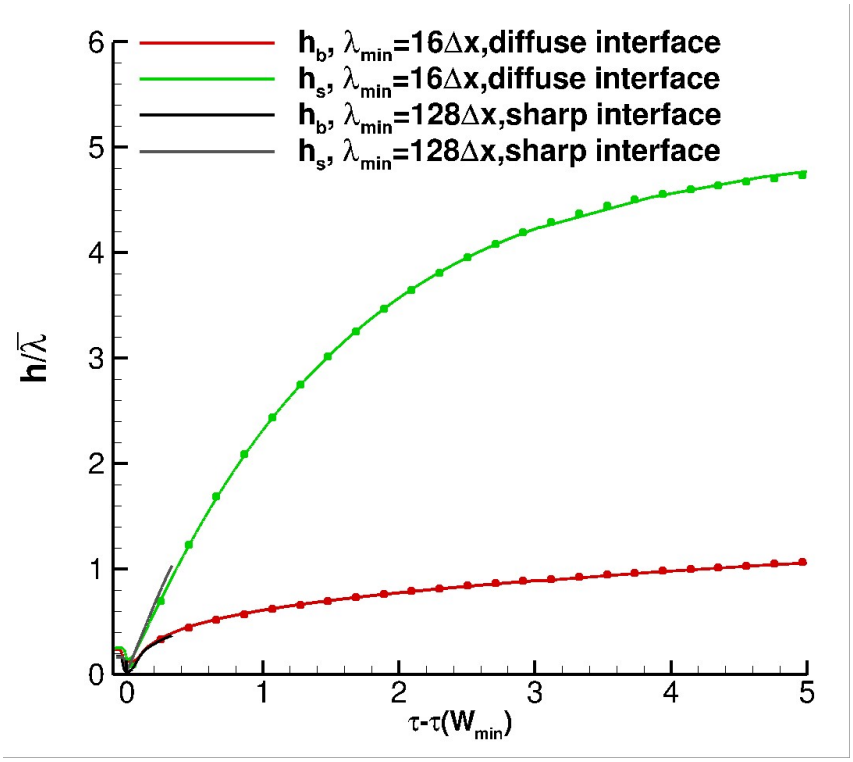

(a)

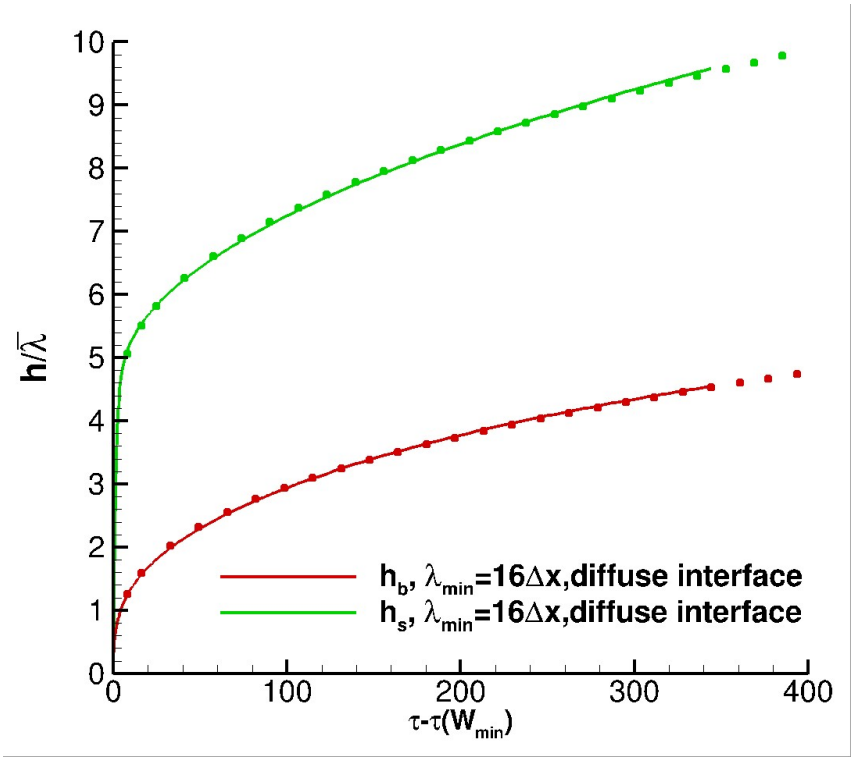

(b)

Fig.24 Application of the Buoyancy-Drag model to the FLAMENCO data, calculations #10, 11. Bubble and spike distances for the high Atwood number case. (a) early time, (b)

late time. Solid lines: iLES data, calculations #10,11. Dots: optimised buoyancy-drag model

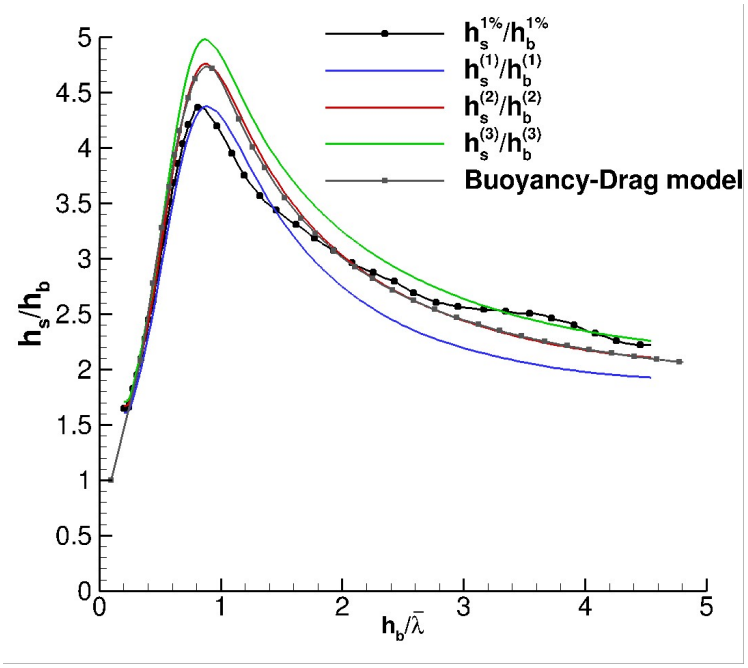

Fig.25 The spike to bubble ratio, h_s / h_b. Comparison of buoyancy-drag model with the iLES data, calculation #10.

9. Concluding remarks

The previous paper [6] showed how iLES data for the integral width (W) could be analyzed to formulate the modifications to the Buoyancy-Drag model needed to give an accurate representation of the influence of the initial conditions for first-shock RM mixing. A narrow-band case was considered, where a suitable mean initial wavelength, $\bar{\lambda}$, can be defined and the pre-shock density ratio was $\rho_1 / \rho_2 = 3$. The analysis involved calculating, directly from the iLES data, the effective length scale, $\ell^{eff} = f\left(\bar{\lambda}, W\right)$, needed in the drag term in the equation for W. The present paper has extended the analysis to use of the Buoyancy-Drag model for separate bubble and spike equations at two density ratios, $\rho_1 / \rho_2 = 3$ and 20.

In some earlier papers, the form used for the Buoyancy-Drag model for post-shock RM is

$$\frac{dV}{dt} = -C_D \frac{V^2}{W}, \quad \frac{dV_b}{dt} = -C_D \frac{V_b^2}{h_b}, \quad \frac{dV_s}{dt} = -C_D \frac{V_s^2}{Rh_b} \quad \text{where } V = \dot{W},\ V_b = \dot{h}_b,\ V_s = \dot{h}_s \qquad (34)$$

$C_D = (1-\theta)/\theta$ and R is the late-time self-similar value of h_s / h_b. In order to represent the influence of the initial conditions the equations are modified to give

$$\frac{dV}{dt} = -\frac{V^2}{\ell^{eff}}, \quad \frac{dV_b}{dt} = -\frac{V_b^2}{\ell_b^{eff}}, \quad \frac{dV_s}{dt} = -\frac{V_s^2}{\ell_s^{eff}} \tag{35}$$

where $\ell^{eff}, \ell_b^{eff}, \ell_s^{eff}$ are functions of $\bar{\lambda}$ and W or h_b. The effective length scales are calculated directly from the iLES data and then approximated by suitable functional forms, equations (30), (32), (33). The functional forms used at late time are

$$\frac{\ell^{eff}}{\bar{\lambda}} = \frac{\theta}{1-\theta}\left(\frac{W}{\bar{\lambda}} - d\right), \quad \frac{\ell_b^{eff}}{\bar{\lambda}} = \frac{\theta}{1-\theta}\left(\frac{h_b}{\bar{\lambda}} - d_b\right), \quad \frac{\ell_s^{eff}}{\bar{\lambda}} = \frac{\theta}{1-\theta}R\left(\frac{h_b}{\bar{\lambda}} - d_s\right) \tag{36}$$

and when $W, h_b \gg \bar{\lambda}$ these forms reduce to (34).

Novel integral definitions of the bubble and spike distances have been devised which vary smoothly with time (required for the computation of ℓ_b^{eff} and ℓ_s^{eff}) and are close to the commonly used definitions based on volume fraction cut-offs. The iLES results show that the spike-to-bubble ratios increase to high values at early time and then fall to much lower values at the end of the simulation. The data used here suggests $R = h_s / h_b \sim 1.1$ *at* $\rho_1 / \rho_2 = 3$ and $R = h_s / h_b \sim 2$ *at* $\rho_1 / \rho_2 = 20$ for the late-stage self-similar state. Experimental results [7] have indicated $\theta_s > \theta_b$ at high density ratios. There is no evidence for this from the calculations analyzed here and the data can be accurately modelled with a common value of θ at each density ratio. In many earlier papers, θ was estimated by fitting the formula $W = A(t - t_0)^{\theta}$ to the late stage data and this assumes that equation (26) was valid for the data range used. As d, d_b, d_s in equation (35) are found to be positive constants the method for estimating θ used here gives slightly higher values, as explained in section 7.3. The estimates for θ are considered to be the best values for the late stages of the simulations, $W / \bar{\lambda} > \sim 0.5$ where ℓ^{eff} is increasing with time. For $\rho_1 / \rho_2 = 3$ vales of θ are in the range 0.30 to 0.37. The iLES for $\rho_1 / \rho_2 = 20$, which has not run to such a late stage as the lower Atwood number calculations, has given values of θ in the range 0.33 to 0.39 . The values of θ are consistent with the theoretical value of $\theta_b = 1/3$ given by [17] for the narrowband case but are greater than the experimental estimates of $\theta_b = 0.25 \pm 0.05$ [7]. The corrected

form of the Buoyancy-Drag model gives accurate fits to the data for W, h_b and h_s over the whole time range with θ=1/3 for $\rho_1 / \rho_2 = 3$ and θ=0.35 for $\rho_1 / \rho_2 = 20$. There is still much uncertainty in the computed values of θ for self-similar mixing. There is significant uncertainty in the best estimates of the slopes in the plots of ℓ^{eff} versus W used to calculate θ. In order to obtain reliable values, iLES needs to be run to a much later stage to get closer to the self-similar state and be sure that the late time slope is achieved. However, this requires a major increase in computer resources.

For the integral mix width, *W*, the modifications to the Buoyancy-Drag model at the two density ratios are similar and equation(25) for $\ell^{eff} = f\left(\bar{\lambda}, W\right)$, as used in [6], gives satisfactory results at both density ratios. For the purpose of engineering modelling a simple prescription which can be used for a wide range of cases is required and this should be feasible for the integral width. On the other hand, the behavior of the bubble and spikes at early time is very different at the two density ratios and a simple prescription has yet to be found. A possible solution is to integrate the Buoyancy-Drag model up to the required time and then use simple approximations for h_b / W and h_s / h_b .

For all the simulations considered here non-linear correction factors, $F_W^{nl}, F_b^{nl}, F_s^{nl}$ have proved necessary. Further simulations are needed to fully understand the variation with initial amplitude. Furthermore, according to the single-mode theory of Velikovich et al. [37] for the incompressible impulsive case , $F_b^{nl}(A) = F_s^{nl}\left(-A\right)$, where the change in the sign of the Atwood number, A , is equivalent to a change of shock direction. In all the cases considered here the shock has travelled from the heavy to the light fluid. The light-to-heavy case also needs to be investigated.

All the results given in this paper are for the narrowband case with $\lambda_{\max} = 2\lambda_{\min}$. This is an idealized test case which should give the lowest value of θ. In experiments, broadband spectra are more likely with higher amplitudes at lower wavenumbers, possibly of the form $P(k) \sim k^{-m}$ with $m > 0$ According to [8,16] , self-similar mixing should then evolve with $\theta = 2/\left(5 - m\right)$. Many shock-driven experiments [13,14,15] have given higher values up to $\theta \sim$ 0.6 which may be explained broadband initial conditions of this type. A similar type of analysis is needed for broadband perturbations. However, in this case there may no longer be a clearly defined initial value of $\bar{\lambda}$ and the range of

perturbation inversion times, $t_{inv} = 1/\left(kA^{+}\Delta u\right)$, will be very large. The modifications to the Buoyancy-Drag model are then likely take on different form. In the cases considered here the unperturbed fluid densities after shock passage, ρ_1^+, ρ_2^+ , remain constant. In applications, they may change due to compression or de-compression. This also needs to be allowed for in the Buoyancy-Drag model and the use of iLES to validate the modifications needed should be carried out. Modifications to the Buoyancy-Drag model for the influence of initial conditions on Rayleigh-Taylor mixing with constant g could also be considered. It is likely that the model for narrowband initial perturbations would be similar to that for the RM case. However, this needs to be confirmed by iLES.

It is clear that accurate representation of the influence of initial conditions in any form of engineering model is a significant challenge.

References

[1] P. Amendt, J.D. Colvin, R.E. Tipton, D.E. Hinkel, M.J. Edwards, O.L. Landen, J.D. Ramshaw, L.J. Suter, W. S. Varnum and R.G. Watt, Indirect-drive Noncryogenic Double-shell Ignition Targets for the National Ignition Facility: Design and Analysis, Phys. Plasmas 9 (2002) 2221–2233. https://doi.org/10.1063/1.1459451.

[2] D.S. Clark, C.R. Weber, J.L. Milovich, J.D. Salmonson, A.L. Kritcher, S.W. Haan, B.A. Hammel, D.E. Hinkel, O.A. Hurricane, O.S. Jones, M.M Marinak, Three-dimensional simulations of low foot and high foot implosion experiments on the National Ignition Facility, Physics of Plasmas 23 (2016) 056302. https://doi.org/10.1063/1.4943527

[3] B. Fryxell, D. Arnett, E. Mueller, Instabilities and clumping in SN 1987A: I. Early evolution in two dimensions, Astrophys. J. 367 (1991) 619-634. https://doi.org/10.086/169657.

[4] Y. Zhou, Rayleigh-Taylor and Richtmyer-Meshkov instability induced flow, turbulence, and mixing. Parts I and II , Physics Reports 720-722 (2017) 1-136 and 723-725 (2017) 1-160. https://doi.org/10.1016/j.physrep.2017.07.005 , https://doi.org/10.1016/j.physrep.2017.07.008 .

[5] B. Thornber, J, Griffond, O. Poujade, N. Attal, H. Varshochi, Bigdelou, P. Ramaprabhu, B. Olson, J. Greenough, Y. Zhou,O. Schilling, K.A Garside, R.J.R. Williams, C.A. Batha, P.A. Kuchugov, M.E Ladonkina, V.F. Tishkin, N.V. Zmitrenko, V.B Rozanov, D.L Youngs, Late-time growth rate, mixing, and anisotropy in the multimode narrowband Richtmyer–Meshkov instability: The θ-group collaboration, Phys. Fluids 29 (2017) 105107. https://doi.org/10.1063/1.4993464.

[6] D. L. Youngs and B. Thornber, Early time modifications to the Buoyancy-Drag model for Richtmyer-Meshkov mixing, submitted to ASME J. Fluids Eng. (2019)

[7] G. Dimonte, M. Schneider, Density ratio dependence of RayleighTaylor mixing for sustained and impulsive acceleration histories, Phys. Fluids, **12** (2000) 304-321. http://dx.doi.org/10.1063/1.870309.

[8] B. Thornber, D. Drikakis, D.L. Youngs, R.J.R. Williams,The influence of initial conditions on turbulent mixing due to Richtmyer–Meshkov instability, J. Fluid Mech. 654 (2010) 99-139. http://dx.doi.org/10.1017/S0022112010000492.

[9] D. Layzer, On the instability of superposed fluids in a gravitational field. Astrophysical Journal 122 (1955) 1-12.

[10] L. Baker, J.R. Freeman, Heuristic model of the nonlinear Rayleigh-Taylor instability, J. Applied Physics 52 (1981) 655-663. https://doi.org/10.1063/1.328793

[11] J.C.V Hansom, P.A Rosen, T.J. Goldsack, K. Oades, P. Fieldhouse, N .Cowperthwaite, D.L Youngs, N. Mawhinney, A.J. Baxter, Radiation driven planar foil instability and mix experiments at the AWE HELEN laser, Laser and Particle Beams 8 (1990) 51-71. https://doi.org/10.1017/S0263034600007825

[12] K. I. Read, Experimental investigation of turbulent mixing by Rayleigh-Taylor instability, Physica D 12 (1984) 45-58. https://doi.org/10.1016/0167-2789(84)90513-X

[13] G. Dimonte, C. E. Frerking, M. Schneider, Richtmyer-Meshkov instability in the turbulent regime, Phys. Rev. letters 74 (1995) 4855- https://doi.org/10.1103/PhysRevLett.74.4855

[14] J. W. Jacobs, V. V. Krivets, V. Tsiklashvili, O. A. Likhachev, Experiments on the Richtmyer–Meshkov instability with an imposed, random initial perturbation, Shock Waves 23 (2013) 407-413. https://doi.org/10.1007/s00193-013-0436-9

[15] V. V Krivets, K. J. Ferguson and J. W. 2017, Turbulent mixing induced by Richtmyer-Meshkov instability, in AIP Conference Proceedings, 1793 (2017),150003. https://doi.org/10.1063/1.4971732

[16] O. Soulard, F. Guillois, J. Griffond, V. Sabelnikov and S. Simoens, Permanence of large eddies in Richtmyer-Meshkov turbulence with a small Atwood number, Phys. Rev. Fluids, 3 (2018), 104603. https://doi.org/10.1103/PhysRevFluids.3.104603

[17] Y. Elbaz, D. Shvarts, Modal model mean field self-similar solutions to the asymptotic evolution of Rayleigh-Taylor and Richtmyer-Meshkov instabilities and its dependence on the initial conditions, Physics of Plasmas 25 (2018) 062126. https://doi.org/10.1063/1.5031922

[18] U. Alon, J. Hecht, D. Ofer and D. Shvarts, Power laws and similarity of Rayleigh-Taylor and Richtmyer-Meshkov mixing fronts at all density ratios. Physical review letters 74 (1995) 534-537. https://doi.org/10.1103/PhysRevLett.74.534

[19] D. Kartoon, D. Oron, L. Arazi, D. Shvarts, Three-dimensional multimode Rayleigh–Taylor and Richtmyer–Meshkov instabilities at all density ratios, Laser and Particle Beams 21 (2003) 327-334. https://doi.org/10.1017/S0263034603213069

[20] J.D Ramshaw, Simple model for linear and nonlinear mixing at unstable fluid interfaces with variable acceleration, Physical review E 58 (1998) 5834 –5840. https://doi.org/10.1103/PhysRevE.58.5834

[21] R.D Richtmyer, Taylor instability in shock acceleration of compressible fluids, Communications on Pure and Applied Mathematics 13 (1960) 297-319. http://dx.doi.org/10.1002/cpa.3160130207

[22] Meyer, K.A. and Blewett, P.J., 1972. “Numerical Investigation of the Stability of a Shock-Accelerated Interface between Two Fluids”, The Physics of Fluids, **15**, pp.753-759. https://doi.org/10.1063/1.1693980 .

[23] M. Vandenboomgaerde, C. Mügler, S. Gauthier, Impulsive model for the Richtmyer-Meshkov instability, Physical Review E 58 (1998) 1874-1882. https://doi.org/10.1103/PhysRevE.58.1874

[24] M.G. Probyn, R.J.R Williams, B. Thornber, D. Drikakis and D.L. Youngs, 2D single-mode Richter-Meshkov Instability, submitted to this issue of PhysicaD (2019).

[25] Y. Zhou, W.H. Cabot and B. Thornber, Asymptotic behavior of the mixed mass in Rayleigh–Taylor and Richtmyer–Meshkov instability induced flows. Physics of Plasmas 23 (2016) 052712. https://doi.org/10.1063/1.4951018

[26] D.L Youngs, Application of monotone integrated large eddy simulation to Rayleigh–Taylor mixing, Phil. Trans. Roy. Soc. A 367 (2009) 2971-2983. https://doi.org/10.1098/rsta.2008.0303

[27] D.L Youngs, The density ratio dependence of self-similar Rayleigh–Taylor mixing, Phil. Trans. Roy. Soc. A 371 (2013) 20120173. http://dx.doi.org/10.1098/rsta.2008.0303.

[28] Thornber, B. and Zhou, Y., 2012 “Energy transfer in the Richtmyer-Meshkov instability,” Phys. Rev. E 86, 056302. https://doi.org/10.1103/PhysRevE.86.056302.

[29] Thornber, B., Mosedale, A., Drikakis, D., Youngs, D.L. and Williams, R.J.R., 2008, “An improved reconstruction method for compressible flows with low Mach number features,” J. Comp. Phys., **227**, pp4873–4894. https://doi.org/10.1016/j.jcp.2008.01.036.

[30] B. Thornber, Impact of domain size and statistical errors in simulations of homogeneous decaying turbulence and the Richtmyer-Meshkov instability, Phys. Fluids 28 (2016) 045106. https://doi.org/10.1063/1.4944877

[31] D. L. Youngs, D.L., 1994, “Numerical simulation of mixing by Rayleigh–Taylor and Richtmyer–Meshkov instabilities”, Laser and particle beams, **12** , pp.725-750. https://doi.org/10.1017/S0263034600008557

[32] Zabusky, N.J., 1999. Vortex paradigm for accelerated inhomogeneous flows: Visiometrics for the Rayleigh-Taylor and Richtmyer-Meshkov environments. *Annual review of fluid mechanics*, *31*(1), pp.495-536. https://doi.org/10.1146/annurev.fluid.31.1.495

[33] Y. Zhou, M. Groom and B. Thornber, Dependence of enstrophy transport and mixed mass on dimensionality and initial conditions in the Richtmyer-Meshkov instability induced flows, submitted to ASME J. Fluids Eng. (2019).

[34] U. Alon, J. Hecht, D. Ofer, and D. Shvarts, Power Laws and Similarity of Rayleigh-Taylor and Richtmyer-Meshkov Mixing Fronts at All Density Ratios, Phys. Rev. Lett. 74 (1995) 534-537. https://doi.org/10.1103/PhysRevLett.74.534

[35] G. Dimonte, G. and P. Ramaprabhu, Simulations and model of the nonlinear Richtmyer–Meshkov instability, Physics of Fluids 22 (2010) 014104. https://doi.org/10.1063/1.3276269

[36] W.T Buttler, D.M. Oró, D.L.Preston, K.O. Mikaelian, F.J. Cherne, R.S. Hixson, R.S., F.G. Mariam,C. Morris, J.B. Stone, G. Terrones and D. Tupa, Unstable Richtmyer–Meshkov growth of solid and liquid metals in vacuum. Journal of Fluid Mechanics, 703 (2012) 60-84. https://doi.org/10.1017/jfm.2012.190

[37] A.L.Velikovich, M. Herrmann and S.I. Abarzhi, Perturbation theory and numerical modelling of weakly and moderately nonlinear dynamics of the incompressible Richtmyer–Meshkov instability, Journal of fluid mechanics 751 (2014) 432-479. https://doi.org/10.1017/jfm.2014.312 .